

# Convolutional equivalent layer for magnetic data processing

Diego Takahashi<sup>†</sup>, Vanderlei C. Oliveira Jr.<sup>†\*</sup> and Valéria C. F. Barbosa<sup>†</sup>

<sup>†</sup>*Observatório Nacional, Department of Geophysics, Rio de Janeiro, Brazil*

\* Corresponding author: *vanderlei@on.br*

(June 17, 2021)

GEO-XXXX

Running head: Magnetic convolutional equivalent layer

## ABSTRACT

## INTRODUCTION

Equivalent layer background:

Dampney (1969), Blakely (1996), Emilia (1973), Li et al. (2014)

Fast methods for equivalent layer:

Leão and Silva (1989), Mendonça and Silva (1994), Oliveira Jr. et al. (2013), Li and Oldenburg (2010), Siqueira et al. (2017), Mendonça (2020)

Methods for solving Toeplitz matrices:

Golub and Loan (2013), Levinson (1946), Chan and Jin (2007)

Toeplitz matrices in Potential methods:

Zhang and Wong (2015), Zhang et al., 2016, Hogue et al. (2020), Renaut et al. (2020)

Convolutional equivalent layer grav:

Siqueira et al. (2017), Takahashi et al. (2020)

About this work:

## METHODOLOGY

### The total-field anomaly

The Earth's magnetic field is commonly divided in three parts: main field, crustal field and external field. The main field is generated in the outer core in a process of self-sustaining dynamo, the crustal field is generated by magnetic bodies in the lithosphere and the external field is generated by electrical currents in the ionosphere and magnetosphere. For exploration geophysics, the crustal field is the object of study, which makes the separation of this data from the acquisition dataset a very important step.

The combination of the main field and crustal field is known as internal field or total-field. Taking the difference between this internal field and the main field given by a model (e.g. IGRF), at the same location, we have the total-field anomaly.

Let  $(x_i, y_i, z_i), i = 1, 2, 3, \dots, N$ , be a observed dataset in a region considering a right-handed Cartesian coordinate system with the  $x$ -axis pointing north,  $y$ -axis pointing east and  $z$ -axis pointing downward. The total-field anomaly at the  $i$ th observation can be approximated to:

$$\Delta T(x_i, y_i, z_i) = \hat{\mathbf{F}}^\top \mathbf{B}(x_i, y_i, z_i), \quad (1)$$

where,  $\mathbf{B}(x_i, y_i, z_i)$  is the crustal field,  $\hat{\mathbf{F}}^\top$  is the transposed unitary vector with the main field directions, with  $\hat{\mathbf{F}}$  described as:

$$\hat{\mathbf{F}} = \begin{bmatrix} F_x \\ F_y \\ F_z \end{bmatrix} = \begin{bmatrix} \cos(I_0) \cos(D_0) \\ \cos(I_0) \sin(D_0) \\ \sin(I_0) \end{bmatrix}, \quad (2)$$

where  $I_0$  is the inclination and  $D_0$  the declination of the main field, respectively.

Considering a uniform magnetized body with volume  $v$  and a total magnetization vector  $\mathbf{m}$ , the induced magnetic field is:

$$\mathbf{B}(x_i, y_i, z_i) = c_m \frac{\mu_0}{4\pi} \mathbf{M}(x_i, y_i, z_i) \mathbf{m}, \quad (3)$$

where,  $\mu_0 = 4\pi 10^{-7}$  H/m is the magnetic constant,  $c_m = 10^9$  is a constant that transforms the induced magnetic field from Tesla (T) to nanotesla (nT) and  $\mathbf{M}(x_i, y_i, z_i)$  is a  $3 \times 3$  matrix given by:

$$\mathbf{M}(x_i, y_i, z_i) = \begin{bmatrix} \partial_{xx}\phi(x_i, y_i, z_i) & \partial_{xy}\phi(x_i, y_i, z_i) & \partial_{xz}\phi(x_i, y_i, z_i) \\ \partial_{xy}\phi(x_i, y_i, z_i) & \partial_{yy}\phi(x_i, y_i, z_i) & \partial_{yz}\phi(x_i, y_i, z_i) \\ \partial_{xz}\phi(x_i, y_i, z_i) & \partial_{yz}\phi(x_i, y_i, z_i) & \partial_{zz}\phi(x_i, y_i, z_i) \end{bmatrix}, \quad (4)$$

where,  $\partial_{\alpha\beta}\phi(x_i, y_i, z_i)$  with  $\alpha = x, y, z$  and  $\beta = x, y, z$ , are the second derivatives of the function  $\phi(x_i, y_i, z_i)$  with respect to  $x, y$  and  $z$ :

$$\phi(x_i, y_i, z_i) = \int_v \int \int \frac{1}{r} dv, \quad (5)$$

where the function  $\frac{1}{r}$  is given by:

$$\frac{1}{\sqrt{(x_i - x_j)^2 + (y_i - y_j)^2 + (z_i - z_j)^2}} \quad (6)$$

and  $x_j, y_j, z_j$  are the  $j$ th Cartesian coordinates within the volume elements of the magnetized body with volume  $v$ , where the integral (equation 5) is conducted.

Rewriting the equation 1 using the magnetic induction given by equation 3 the total-field anomaly  $\Delta T(x, y, z)$  is given by:

$$\Delta T(x_i, y_i, z_i) = c_m \frac{\mu_0}{4\pi} m \hat{\mathbf{F}}^\top \mathbf{M}(x_i, y_i, z_i) \hat{\mathbf{m}}, \quad (7)$$

where  $m$  is the magnetization intensity and  $\hat{\mathbf{m}}$  is the directional unitary vector.

## Equivalent layer for magnetic data

Grounded on the equivalent layer principle it is possible to calculate the total-field anomaly  $\Delta T(x_i, y_i, z_i)$  (equation 7) with the convolution between the harmonic function and the physical property:

$$\Delta T(x_i, y_i, z_i) = \int_{-\infty}^{+\infty} \int_{-\infty}^{+\infty} p(x_j, y_j, z_c) \left[ c_m \frac{\mu_0}{4\pi} \hat{\mathbf{F}}^\top \mathbf{H} \hat{\mathbf{h}} \right] dx dy, \quad (8)$$

where  $z_c$  is a constant representing the depth of the equivalent layer with  $z_i < z_c$ . The unitary vector  $\hat{\mathbf{h}}$  is the magnetization directions of the equivalent sources over the layer:

$$\hat{\mathbf{h}} = \begin{bmatrix} h_x \\ h_y \\ h_z \end{bmatrix} = \begin{bmatrix} \cos(I) \cos(D) \\ \cos(I) \sin(D) \\ \sin(I) \end{bmatrix}, \quad (9)$$

where  $I$  and  $D$  are, respectively, the inclination and declination of the equivalent sources,  $\mathbf{H}$  is a  $3 \times 3$  matrix that contains the second derivatives in relation to the observed Cartesian coordinates  $x, y, z$  as presented in equation 6:

$$\mathbf{H} = \begin{bmatrix} \partial_{xx} \frac{1}{r} & \partial_{xy} \frac{1}{r} & \partial_{xz} \frac{1}{r} \\ \partial_{xy} \frac{1}{r} & \partial_{yy} \frac{1}{r} & \partial_{yz} \frac{1}{r} \\ \partial_{xz} \frac{1}{r} & \partial_{yz} \frac{1}{r} & \partial_{zz} \frac{1}{r} \end{bmatrix} = \begin{bmatrix} H_{xx} & H_{xy} & H_{xz} \\ H_{xy} & H_{yy} & H_{yz} \\ H_{xz} & H_{yz} & H_{zz} \end{bmatrix}, \quad (10)$$

and the physical property  $p(x_j, y_j, z_c)$  represents the magnetic dipole moment distribution over the layer and has unit of  $Am^2$ .

Discretizing equation 8 we get:

$$\Delta T(x_i, y_i, z_i) = \sum_{j=1}^M p_j a_{ij}, \quad (11)$$

where  $j = 1, 2, 3, \dots, M$  are the equivalent sources discretized and distributed across the layer and  $a_{ij}$  is given by:

$$a_{ij} = c_m \frac{\mu_0}{4\pi} \hat{\mathbf{F}}^\top \mathbf{H}_{ij} \hat{\mathbf{h}}. \quad (12)$$

Equation 11 can be written as:

$$\mathbf{d}(\mathbf{p}) = \mathbf{A}\mathbf{p}, \quad (13)$$

where  $\mathbf{d}(\mathbf{p})$  is the vector of total-field anomaly,  $\mathbf{A}$  is a matrix containing the elements given by equation 12, also known as the sensitivity matrix and  $\mathbf{p}$  is the vector containing the dipole moments of each equivalent source. By using the normal equations:

$$\mathbf{A}^\top \mathbf{A}\mathbf{p} = \mathbf{A}^\top \mathbf{d}^o \quad (14)$$

which is a conventional manner of solving linear systems, the estimative of the dipole moment parameters vector can be calculated from the total-field anomaly as:

$$\hat{\mathbf{p}} = (\mathbf{A}^\top \mathbf{A})^{-1} \mathbf{A}^\top \mathbf{d}^o \quad (15)$$

where  $\mathbf{d}^o$  is the observed total-field anomaly. Equation 15 will be referenced throughout this work as the classical method for solving the equivalent layer.

### Conjugate Gradient Least Square method (CGLS)

As an alternative from the clasical method of parameter estimative, the conjugate gradient (CG) is a well-known iterative method for solving linear systems with symmetric positive definite matrices. By minimizing the quadratic form:

$$\Phi(\mathbf{p}) = \frac{1}{2} \mathbf{p}^\top \mathbf{A} \mathbf{p} - \mathbf{d}^o \top \mathbf{p}, \quad (16)$$

it is possible to solve the system by constructing a basis of conjugate directions  $c \in R^N$  (Aster et al., 2018). As we are solving a general least square problem and matrix  $\mathbf{A}$  (equation 12) is not symmetric, instead we minimize:

$$\|\mathbf{A} \mathbf{p} - \mathbf{d}^o\|_2, \quad (17)$$

by applying the conjugate gradient to the normal equations (equation 14).

In theory, this method is bound to converge at  $N$  iterations maximum, but in a later part of this work we show with numerical results that the convergence is much faster for the linear system we are solving.

A pseudocode for the CGLS method follows:

---

**Algorithm 1** Conjugate Gradient Least Square pseudocode (Aster et al., 2018, p. 166).

---

Input:  $\mathbf{A} \in R^{N \times M}$  and  $\mathbf{d}^o \in R^N$ .

Output: Estimative of parameter vector  $\hat{\mathbf{p}}$ .

Let  $it = 0$ ,  $\hat{\mathbf{p}}^{(0)} = \mathbf{0}$ ,  $\mathbf{c}^{(-1)} = \mathbf{0}$ ,  $\beta_0 = 0$ ,  $\mathbf{s}^{(0)} = \mathbf{d}^o - \mathbf{A}\hat{\mathbf{p}}^{(0)}$  and  $\mathbf{r}^{(0)} = \mathbf{A}^\top \mathbf{s}^{(0)}$ .

$$1 - \text{If } it > 0, \text{ let } \beta_{(it)} = \frac{\mathbf{r}^{(it)\top} \mathbf{r}^{(it)}}{\mathbf{r}^{(it-1)\top} \mathbf{r}^{(it-1)}}$$

$$2 - \mathbf{c}^{(it)} = \mathbf{r}^{(it)} - \alpha_{(it)} \beta_{(it)} \mathbf{c}^{(it-1)}.$$

$$3 - \alpha_{(it)} = \frac{\|\mathbf{r}^{(it)}\|_2^2}{(\mathbf{c}^{(it)\top} \mathbf{A}^\top)(\mathbf{A} \mathbf{c}^{(it)})}.$$

$$4 - \hat{\mathbf{p}}^{(it+1)} = \hat{\mathbf{p}}^{(it)} - \alpha_{(it)} \mathbf{c}^{(it)}.$$

$$5 - \mathbf{s}^{(it+1)} = \mathbf{s}^{(it)} - \alpha_{(it)} \mathbf{A} \mathbf{c}^{(it)}.$$

$$6 - \mathbf{r}^{(it+1)} = \mathbf{A}^\top \mathbf{s}^{(it+1)}.$$

$$7 - it = it + 1.$$

$$8 - \text{Repeat previous steps until convergence.}$$


---

Different from the classical least-square solution (equation 15), the CGLS solution (Algorithm 1) requires neither inverse matrix nor matrix-matrix product. The CGLS method only requires: one matrix-vector multiplication out of the loop and two matrix-vector multiplications, in steps 3 and 6, at each iteration.

In this work, we will reduce the computational cost of the equivalent layer by substituting exactly these two matrix-vector products with a much more efficient algorithm.

## Non-symmetric Block-Toeplitz Toeplitz-Block structure of matrix A

Let us consider that the observed total-field anomaly is located on an  $N_x \times N_y$  regular grid of points spaced by  $\Delta_x$  and  $\Delta_y$  along the  $x$ - and  $y$ -directions, respectively. The notation used in this work will be the same as the one presented in Takahashi et al. (2020), where the authors described the structure of the symmetric Block-Toeplitz Toeplitz-Block matrix of the gravimetric equivalent layer. Here, we also establish a relation between the pair of *matrix coordinates*  $(x_i, y_i)$ ,  $i = 1, \dots, N$  or  $(x_j, y_j)$ ,  $j = 1, \dots, M = N$  and a pair of *grid coordinates*  $(x_k, y_l)$  given as:

$$x_i \equiv x_k = x_1 + [k(i) - 1] \Delta x , \quad (18)$$

and

$$y_i \equiv y_l = y_1 + [l(i) - 1] \Delta y . \quad (19)$$

In a *x-oriented grid* the indices  $i$  (or  $j$ ) relate as integer functions of  $k$  and  $l$  by:

$$i(k, l) = (l - 1) N_x + k , \quad (20)$$

$$l(i) = \left\lceil \frac{i}{N_x} \right\rceil \quad (21)$$

and

$$k(i) = i - \left\lceil \frac{i}{N_x} \right\rceil N_x + N_x . \quad (22)$$

For *y-oriented grid* they are given by:

$$i(k, l) = (k - 1) N_y + l , \quad (23)$$

$$k(i) = \left\lceil \frac{i}{N_y} \right\rceil \quad (24)$$

and

$$l(i) = i - \left\lceil \frac{i}{N_y} \right\rceil N_y + N_y , \quad (25)$$

where in equations 21 to 25,  $\lceil \cdot \rceil$  is the ceiling function. Figure 1 shows an example of a grid  $N_x \times N_y$ , where  $N_x = 4$  and  $N_y = 3$  demonstrating the relation between the *matrix coordinates* with  $k(i)$  and  $l(i)$  depending on the orientation of the grid.

The  $N \times M$  sensitivity matrix  $\mathbf{A}$  (equation 12) can be represented as a grid of  $Q \times Q$  blocks  $\mathbf{A}^q$ ,  $q = -Q + 1, \dots, 0, \dots, Q - 1$ . Each block  $\mathbf{A}^q$  has  $P \times P$  elements  $a_p^q$  where  $p = -P + 1, \dots, 0, \dots, P - 1$

In a *x-oriented grid*  $q$  and  $p$  give the number of blocks ( $Q = N_y$ ) and the number of elements of each block ( $P = N_x$ ). They can be defined by the integer functions:

$$q(i, j) = l(i) - l(j) \quad (26)$$

and

$$p(i, j) = k(i) - k(j), \quad (27)$$

where equations 21 and 22 describe  $l(i)$  and  $l(j)$  and  $k(i)$  and  $k(j)$ , respectively. When using *y-oriented grids*,  $q$  and  $p$  still define the number of block and block elements, but  $Q = N_x$  and  $P = N_y$ . Moreover, the integer functions changes to:

$$q(i, j) = k(i) - k(j) \quad (28)$$

and

$$p(i, j) = l(i) - l(j), \quad (29)$$

where equation 24 now defines  $k(i)$  and  $k(j)$  and equation 25 defines  $l(i)$  and  $l(j)$ . Note that equations 26, 27, 28 and 29 differs from the ones presented in Takahashi et al. (2020) by the absence of the module.

In both *x-* or *y-orientation*, matrix  $\mathbf{A}$  (equation 12) can be rewritten by the indices

$q = -Q + 1, \dots, 0, \dots, Q - 1$  defining the number of its blocks:

$$\mathbf{A} = \begin{bmatrix} \mathbf{A}^0 & \mathbf{A}^{-1} & \cdots & \mathbf{A}^{-Q+1} \\ \mathbf{A}^1 & \mathbf{A}^0 & \mathbf{A}^{-1} & \vdots \\ \vdots & \mathbf{A}^1 & \ddots & \mathbf{A}^{-1} \\ \mathbf{A}^{Q-1} & \cdots & \mathbf{A}^1 & \mathbf{A}^0 \end{bmatrix}_{N \times N}, \quad (30)$$

and by indice  $p$ , where each block has  $P \times P$  elements  $a_p^q$ ,  $p = -P + 1, \dots, 0, \dots, P - 1$ :

$$\mathbf{A}^q = \begin{bmatrix} a_0^q & a_{-1}^q & \cdots & a_{-P+1}^q \\ a_1^q & a_0^q & a_{-1}^q & \vdots \\ \vdots & a_1^q & \ddots & a_{-1}^q \\ a_{P-1}^q & \cdots & a_1^q & a_0^q \end{bmatrix}_{P \times P}, \quad (31)$$

In general, matrix  $\mathbf{A}$  (equation 12) is a non-symmetric BTTB, i.e., its blocks are non-symmetric ( $\mathbf{A}^{-Q+1} \neq \mathbf{A}^{Q-1}$ ) and its elements also are non-symmetric ( $a_{-1}^q \neq a_1^q$ ). Depending on specific values of the main field direction and the equivalent sources magnetization directions, matrix  $\mathbf{A}$  can assume other structures, for example, when  $\hat{\mathbf{F}} = [0, 0, 1]$  and  $\hat{\mathbf{h}} = [0, 0, 1]$  it becomes symmetric. In this work, we are considering the more common situation for the matrix  $\mathbf{A}$ .

Also differently for the symmetric sensitivity matrix described by Takahashi et al. (2020), the non-symmetric BTTB matrix cannot be reconstructed only by its first column. The construction of the matrix  $\mathbf{A}$  (equation 12) needs four columns: the first and last columns of the first column of blocks and the first and last columns of the last column of blocks. This has a physical implication in the equivalent layer which is not possible to use only one equivalent source to reproduce all elements of matrix  $\mathbf{A}$ , such as in the gravity case as demonstrated by Takahashi et al. (2020). Rather, in the magnetic case it takes four equivalent sources positioned at each corner of the equivalent layer. Figure 2 shows the

positioning of the equivalent sources in a regular grid  $N_x = 4$   $N_y = 3$  necessary to calculate the four columns capable of recover the matrix  $\mathbf{A}$ .

In this work, we propose a different approach, by calculating the first column of all six different components of second derivatives matrices from  $\mathbf{H}_{ij}$  (equation 10). These matrices are, in fact, symmetrics or skew-symmetrics BTTBs, meaning that the first column has all elements of each matrix.

By substituting equations 2, 9 and 10 into equation 12, it is possible to describe each element of the sensitivity matrix by the second derivative components of  $\mathbf{H}_{ij}$ :

$$\begin{aligned} a_{ij} = c_m \frac{\mu_0}{4\pi} & (F_x H_{xx} + F_y H_{xy} + F_z H_{xz}) h_x + \\ & (F_x H_{xy} + F_y H_{yy} + F_z H_{yz}) h_y + \\ & (F_x H_{xz} + F_y H_{yz} + F_z H_{zz}) h_z . \end{aligned} \quad (32)$$

If we consider that  $c_m \frac{\mu_0}{4\pi}$ ,  $\hat{\mathbf{F}}$  (equation 2) and  $\hat{\mathbf{h}}$  (equation 9) are constants multiplying the second derivatives  $\mathbf{H}$  (equation 10), the sensitivity matrix  $\mathbf{A}$  (equation 12) is purely the sum of the components  $H_{xx} + H_{xy} + H_{xz} + H_{xy} + H_{yy} + H_{yz} + H_{xz} + H_{yz} + H_{zz}$  multiplied by the respectives constants of each component. Thus, despite  $\mathbf{A}$  not being a symmetric BTTB matrix, it can be in fact, written by calculating only the first column of these components.

In the next few sections we will describe each component  $\mathbf{H}$  as its own matrix.

### Structure of matrices components $\mathbf{H}_{xx}$ , $\mathbf{H}_{yy}$ and $\mathbf{H}_{zz}$

We can describe the elements of  $\mathbf{H}_{xx}$ ,  $\mathbf{H}_{yy}$  and  $\mathbf{H}_{zz}$  by substituting equations 18 and 19 in equation 10 as:

$$h_{ij}^{xx} = \frac{-1}{[(\Delta k_{ij} \Delta x)^2 + (\Delta l_{ij} \Delta y)^2 + (\Delta z)^2]^{\frac{3}{2}}} + \frac{3(\Delta k_{ij} \Delta x)^2}{[(\Delta k_{ij} \Delta x)^2 + (\Delta l_{ij} \Delta y)^2 + (\Delta z)^2]^{\frac{5}{2}}}, \quad (33)$$

$$h_{ij}^{yy} = \frac{-1}{[(\Delta k_{ij} \Delta x)^2 + (\Delta l_{ij} \Delta y)^2 + (\Delta z)^2]^{\frac{3}{2}}} + \frac{3(\Delta l_{ij} \Delta y)^2}{[(\Delta k_{ij} \Delta x)^2 + (\Delta l_{ij} \Delta y)^2 + (\Delta z)^2]^{\frac{5}{2}}} \quad (34)$$

and

$$h_{ij}^{zz} = \frac{-1}{[(\Delta k_{ij} \Delta x)^2 + (\Delta l_{ij} \Delta y)^2 + (\Delta z)^2]^{\frac{3}{2}}} + \frac{3(\Delta z)^2}{[(\Delta k_{ij} \Delta x)^2 + (\Delta l_{ij} \Delta y)^2 + (\Delta z)^2]^{\frac{5}{2}}}, \quad (35)$$

where  $\Delta z = z_j - z_i$ ,  $\Delta k_{ij} = k(i) - k(j)$  (equations 22 or 24) and  $\Delta l_{ij} = l(i) - l(j)$  (equations 21 or 25). The principal components  $\mathbf{H}_{xx}$ ,  $\mathbf{H}_{yy}$  and  $\mathbf{H}_{zz}$  (equations 33, 34 and 35, respectively) of matrix  $\mathbf{H}$  (equation 10) are symmetric-Block-Toeplitz symmetric-Toeplitz-Block matrices. This means that  $\mathbf{H}_{xx}$ ,  $\mathbf{H}_{yy}$  and  $\mathbf{H}_{zz}$  are Toeplitz and symmetric by its blocks and each of the blocks are symmetric Toeplitz matrices. For example,  $\mathbf{H}_{xx}$  can be described by the *block indice*  $q$  that represent the block diagonals of this matrix as a grid of  $Q \times Q$  blocks  $\mathbf{H}_{xx}^q$ ,  $q = 0, \dots, Q - 1$ :

$$\mathbf{H}_{xx} = \begin{bmatrix} \mathbf{H}_{xx}^0 & \mathbf{H}_{xx}^1 & \cdots & \mathbf{H}_{xx}^{Q-1} \\ \mathbf{H}_{xx}^1 & \mathbf{H}_{xx}^0 & \ddots & \vdots \\ \vdots & \ddots & \ddots & \mathbf{H}_{xx}^1 \\ \mathbf{H}_{xx}^{Q-1} & \cdots & \mathbf{H}_{xx}^1 & \mathbf{H}_{xx}^0 \end{bmatrix}_{N \times N}. \quad (36)$$

And each diagonal of the blocks are represented by  $P \times P$  elements  $h_p^q$ ,  $p = 0, \dots, P - 1$ :

$$\mathbf{H}_{xx}^q = \{h_p^q\} = \begin{bmatrix} h_0^q & h_1^q & \cdots & h_{P-1}^q \\ h_1^q & h_0^q & \ddots & \vdots \\ \vdots & \ddots & \ddots & h_1^q \\ h_{P-1}^q & \cdots & h_1^q & h_0^q \end{bmatrix}_{P \times P}. \quad (37)$$

In a *x-oriented grid*  $Q = N_x$ ,  $P = N_y$  and  $q$  and  $p$  can be defined by the functions:

$$q(i, j) = |l(i) - l(j)| \quad (38)$$

and

$$p(i, j) = | k(i) - k(j) | , \quad (39)$$

where  $l(i)$  and  $l(j)$  are defined by equation 21 and  $k(i)$  and  $k(j)$  are defined by equation 22. For  $y$ -oriented grids,  $Q = N_x$ ,  $P = N_y$  and the block indices  $q$  and  $p$  are defined, respectively, by the following integer functions of the matrix indices  $i$  and  $j$ :

$$q(i, j) = | k(i) - k(j) | \quad (40)$$

and

$$p(i, j) = | l(i) - l(j) | , \quad (41)$$

This struture can also describe matrices  $\mathbf{H}_{yy}$  and  $\mathbf{H}_{zz}$  in the same manner and they are identical to the structure of the gravity sensitivity matrix from Takahashi et al. (2020).

### Structure of the components matrices $\mathbf{H}_{xy}$

By substituting equations 18 and 19 in equation 10, we can also describe the elements of  $\mathbf{H}_{xy}$ , as:

$$h_{ij}^{xy} = \frac{3(\Delta k_{ij} \Delta x)(\Delta l_{ij} \Delta y)}{\left[ (\Delta k_{ij} \Delta x)^2 + (\Delta l_{ij} \Delta y)^2 + (\Delta z)^2 \right]^{\frac{5}{2}}} , \quad (42)$$

The component  $\mathbf{H}_{xy}$  (equation 42) of matrix  $\mathbf{H}$  (equation 10) are skew symmetric-Block-Toeplitz skew symmetric-Toeplitz-Block matrices. This means that  $\mathbf{H}_{xy}$  is Toeplitz and skew symmetric by its blocks and each of the blocks are skew symmetric Toeplitz matrices. This way, matrix  $\mathbf{H}_{xy}$  can be described by the *block indice*  $q$  that represent the

block diagonals of this matrix as a grid of  $Q \times Q$  blocks  $\mathbf{H}_{\mathbf{xy}}^q$ ,  $q = -Q + 1, \dots, 0, \dots, Q - 1$ :

$$\mathbf{H}_{\mathbf{xy}} = \begin{bmatrix} \mathbf{H}_{\mathbf{xy}}^0 & \mathbf{H}_{\mathbf{xy}}^{-1} & \cdots & \mathbf{H}_{\mathbf{xy}}^{-Q+1} \\ \mathbf{H}_{\mathbf{xy}}^1 & \mathbf{H}_{\mathbf{xy}}^0 & \ddots & \vdots \\ \vdots & \ddots & \ddots & \mathbf{H}_{\mathbf{xy}}^{-1} \\ \mathbf{H}_{\mathbf{xy}}^{Q-1} & \cdots & \mathbf{H}_{\mathbf{xy}}^1 & \mathbf{H}_{\mathbf{xy}}^0 \end{bmatrix}_{N \times N}. \quad (43)$$

And each diagonal of the blocks are represented by  $P \times P$  elements  $h_p^q$ ,  $p = -P + 1, \dots, 0, \dots, P - 1$ :

$$\mathbf{H}_{\mathbf{xy}}^q = \{h_p^q\} = \begin{bmatrix} h_0^q & h_{-1}^q & \cdots & h_{-P+1}^q \\ h_1^q & h_0^q & \ddots & \vdots \\ \vdots & \ddots & \ddots & h_{-1}^q \\ h_{P-1}^q & \cdots & h_1^q & h_0^q \end{bmatrix}_{P \times P}. \quad (44)$$

In a *x-oriented grid*  $Q = N_x$ ,  $P = N_y$  and  $q$  and  $p$  can be defined by the functions:

$$q(i, j) = l(i) - l(j) \quad (45)$$

and

$$p(i, j) = k(i) - k(j) \quad , \quad (46)$$

where  $l(i)$  and  $l(j)$  are defined by equation 21 and  $k(i)$  and  $k(j)$  are defined by equation 22. For *y-oriented grids*,  $Q = N_x$ ,  $P = N_y$  and the block indices  $q$  and  $p$  are defined, respectively, by the following integer functions of the matrix indices  $i$  and  $j$ :

$$q(i, j) = k(i) - k(j) \quad (47)$$

and

$$p(i, j) = l(i) - l(j) \quad , \quad (48)$$

Important to clarify that in this case, as a skew symmetric matrix, the values of oposing diagonals have oposing signals, e.g.,  $\mathbf{H}_{\mathbf{xy}}^{-1} = -\mathbf{H}_{\mathbf{xy}}^1$  and  $h_{-1}^q = -h_1^q$ .

## Structure of the components matrices $\mathbf{H}_{xz}$

By substituting equations 18 and 19 in equation 10, the elements of  $\mathbf{H}_{xz}$ , are given by:

$$h_{ij}^{xz} = \frac{3(\Delta k_{ij} \Delta x)(\Delta z)}{\left[(\Delta k_{ij} \Delta x)^2 + (\Delta l_{ij} \Delta y)^2 + (\Delta z)^2\right]^{\frac{5}{2}}}, \quad (49)$$

The component  $\mathbf{H}_{xz}$  (equation 49) of matrix  $\mathbf{H}$  (equation 10) are skew symmetric-Block-Toeplitz symmetric-Toeplitz-Block matrices. This means that  $\mathbf{H}_{xz}$  is Toeplitz and skew symmetric by its blocks and each of the blocks are symmetric Toeplitz matrices. Thus, matrix  $\mathbf{H}_{xz}$  can be described by the *block indice*  $q$  that represent the block diagonals of this matrix as a grid of  $Q \times Q$  blocks  $\mathbf{H}_{xz}^q$ ,  $q = -Q + 1, \dots, 0, \dots, Q - 1$ :

$$\mathbf{H}_{xz} = \begin{bmatrix} \mathbf{H}_{xz}^0 & \mathbf{H}_{xz}^{-1} & \dots & \mathbf{H}_{xz}^{-Q+1} \\ \mathbf{H}_{xz}^1 & \mathbf{H}_{xz}^0 & \ddots & \vdots \\ \vdots & \ddots & \ddots & \mathbf{H}_{xz}^{-1} \\ \mathbf{H}_{xz}^{Q-1} & \dots & \mathbf{H}_{xz}^1 & \mathbf{H}_{xz}^0 \end{bmatrix}_{N \times N}. \quad (50)$$

And each diagonal of the blocks are represented by  $P \times P$  elements  $h_p^q$ ,  $p = 0, \dots, P - 1$ :

$$\mathbf{H}_{xz}^q = \{h_p^q\} = \begin{bmatrix} h_0^q & h_1^q & \dots & h_{P-1}^q \\ h_1^q & h_0^q & \ddots & \vdots \\ \vdots & \ddots & \ddots & h_1^q \\ h_{P-1}^q & \dots & h_1^q & h_0^q \end{bmatrix}_{P \times P}. \quad (51)$$

In a *x-oriented grid*  $Q = N_x$ ,  $P = N_y$  and  $q$  and  $p$  can be defined by the functions:

$$q(i, j) = l(i) - l(j) \quad (52)$$

and

$$p(i, j) = |k(i) - k(j)|, \quad (53)$$

where  $l(i)$  and  $l(j)$  are defined by equation 21 and  $k(i)$  and  $k(j)$  are defined by equation 22. For  $y$ -oriented grids,  $Q = N_x$ ,  $P = N_y$  and the block indices  $q$  and  $p$  are defined, respectively, by the following integer functions of the matrix indices  $i$  and  $j$ :

$$q(i, j) = k(i) - k(j) \quad (54)$$

and

$$p(i, j) = |l(i) - l(j)| , \quad (55)$$

In this case as a skew symmetric matrix by blocks, the values of oposing diagonals blocks have oposing signals, e.g.,  $\mathbf{H}_{xz}^{-1} = -\mathbf{H}_{xz}^1$  but each block is a symmetric matrix.

### Structure of the components matrices $\mathbf{H}_{yz}$

Finally, by substituting equations 18 and 19 in equation 10, we can also describe the elements of  $\mathbf{H}_{yz}$ , as:

$$h_{ij}^{yz} = \frac{3(\Delta l_{ij} \Delta y)(\Delta z)}{\left[(\Delta k_{ij} \Delta x)^2 + (\Delta l_{ij} \Delta y)^2 + (\Delta z)^2\right]^{\frac{5}{2}}} , \quad (56)$$

The component  $\mathbf{H}_{yz}$  (equation 56) of matrix  $\mathbf{H}$  (equation 10) are symmetric-Block-Toeplitz skew symmetric-Toeplitz-Block matrices. This means that  $\mathbf{H}_{yz}$  is Toeplitz and symmetric by its blocks and each of the blocks are skew symmetric Toeplitz matrices. Thus, matrix  $\mathbf{H}_{yz}$  can be described by the *block indice*  $q$  that represent the block diagonals of this matrix as a grid of  $Q \times Q$  blocks  $\mathbf{H}_{yz}^q$ ,  $q = 0, \dots, Q - 1$ :

$$\mathbf{H}_{yz} = \begin{bmatrix} \mathbf{H}_{yz}^0 & \mathbf{H}_{yz}^1 & \dots & \mathbf{H}_{yz}^{Q-1} \\ \mathbf{H}_{yz}^1 & \mathbf{H}_{yz}^0 & \ddots & \vdots \\ \vdots & \ddots & \ddots & \mathbf{H}_{yz}^1 \\ \mathbf{H}_{yz}^{Q-1} & \dots & \mathbf{H}_{yz}^1 & \mathbf{H}_{yz}^0 \end{bmatrix}_{N \times N} . \quad (57)$$

And each diagonal of the blocks are represented by  $P \times P$  elements  $h_p^q$ ,  $p = -P + 1, \dots, 0, \dots, P - 1$ :

$$\mathbf{H}_{\mathbf{yz}}^q = \{h_p^q\} = \begin{bmatrix} h_0^q & h_{-1}^q & \cdots & h_{-P+1}^q \\ h_1^q & h_0^q & \ddots & \vdots \\ \vdots & \ddots & \ddots & h_{-1}^q \\ h_{P-1}^q & \cdots & h_1^q & h_0^q \end{bmatrix}_{P \times P}. \quad (58)$$

In a *x-oriented grid*  $Q = N_x$ ,  $P = N_y$  and  $q$  and  $p$  can be defined by the functions:

$$q(i, j) = |l(i) - l(j)| \quad (59)$$

and

$$p(i, j) = k(i) - k(j), \quad (60)$$

where  $l(i)$  and  $l(j)$  are defined by equation 21 and  $k(i)$  and  $k(j)$  are defined by equation 22. For *y-oriented grids*,  $Q = N_x$ ,  $P = N_y$  and the block indices  $q$  and  $p$  are defined, respectively, by the following integer functions of the matrix indices  $i$  and  $j$ :

$$q(i, j) = |k(i) - k(j)| \quad (61)$$

and

$$p(i, j) = l(i) - l(j), \quad (62)$$

Being a symmetric matrix by blocks, the values of  $\mathbf{H}_{\mathbf{yz}}$  from oposing diagonals blocks are equal, but each block have skew symmetric oposing diagonals, i.e.,  $h_{-1}^q = -h_1^q$ .

## CGLS matrix-vector substitution

As pointed earlier in this work, the main improvement inside the CGLS method (Algorithm 1) for estimating the parameter vector  $\hat{\mathbf{p}}$  (equation 15) is to substitute the matrix-vector

multiplication  $\mathbf{A}^\top \mathbf{s}^{(0)}$  out of the loop and the two matrix-vector multiplications inside the loop at steps 3 an 6,  $\mathbf{A} \mathbf{c}^{(it)}$  and  $\mathbf{A}^\top \mathbf{s}^{(it+1)}$ , that is necessary at each iteration and takes most of its runtime.

Our method consists in calculating the six first columns of the second derivatives of  $\mathbf{H}$  (equation 10) and embed them into the first six columns of the block-circulant circulant-block (BCCB) matrices related to the  $\mathbf{H}$  components. Thus, it is possible to calculate the first column of the BCCB matrix embedded from matrix  $\mathbf{A}$  (equation 12) by multiplying each component with its respective constants and summing as shown in equation 32. In Takahashi et al. (2020), Appendix A, the authors demonstrated in details how to transform a symmetric BTTB matrix into a BCCB matrix  $\mathbf{C}$ . The process here is the same and that work can be referenced to achieve the same results.

A new auxiliary linear system is constructed to carry the matrix-vector product:

$$\mathbf{w} = \mathbf{C}\mathbf{v}, \quad (63)$$

where

$$\mathbf{w} = \begin{bmatrix} \mathbf{w}_0 \\ \vdots \\ \mathbf{w}_{Q-1} \\ \mathbf{0}_{2N \times 1} \end{bmatrix}_{4N \times 1}, \quad (64)$$

$$\mathbf{w}_q = \begin{bmatrix} \mathbf{d}_q(\mathbf{p}) \\ \mathbf{0}_{P \times 1} \end{bmatrix}_{2P \times 1}, \quad (65)$$

$$\mathbf{v} = \begin{bmatrix} \mathbf{v}_0 \\ \vdots \\ \mathbf{v}_{Q-1} \\ \mathbf{0}_{2N \times 1} \end{bmatrix}_{4N \times 1}, \quad (66)$$

and

$$\mathbf{v}_q = \begin{bmatrix} \mathbf{p}_q \\ \mathbf{0}_{P \times 1} \end{bmatrix}_{2P \times 1}, \quad (67)$$

where  $\mathbf{C}$  (equation 63) is a  $4N \times 4N$  non-symmetric (BCCB) resulted from transforming  $\mathbf{A}$  (equation 12). Without having to calculate the whole BCCB matrix, its first column can be used to carry the multiplication of this new system (equation 63). Appendix A and C in Takahashi et al. (2020) shows how to use the 2D-FFT to compute the eigenvalues of matrix  $\mathbf{C}$ , store in a  $2Q \times 2P$  matrix using the *vec*-operator and to carry the matrix-vector product. Denoting matrix  $\mathbf{L}$  as the eigenvalues matrix follows:

$$\mathbf{F}_{2Q}^* [\mathbf{L} \circ (\mathbf{F}_{2Q} \mathbf{V} \mathbf{F}_{2P})] \mathbf{F}_{2P}^* = \mathbf{W}, \quad (68)$$

where the symbol “ $\circ$ ” references the Hadamard product, i.e., a element-wise complex multiplication between the eigenvalues and the 2D-FFT of the matrix rearranged along the rows of the parameters  $\mathbf{V}$  (equation 66) using the same *vec*-operator. The resulting inverse 2D-FFT denoted by  $\mathbf{F}_{2Q}^* \otimes \mathbf{F}_{2P}^*$  is also a  $2Q \times 2P$  matrix ( $\mathbf{W}$ ) that can be rearranged to the predicted data vector  $\mathbf{d}(\hat{\mathbf{p}})$  size  $N$ .

## Computational performance

To compare the efficiency of our algorithm we will use a numerical approach and calculate the floating-point operations (*flops*), i.e., count the number of mathematical operations necessary to complete the estimative of parameter vector  $\hat{\mathbf{p}}$  of the normal equations (equation

15) and both the CGLS methods (algorithm 1) for calculating the matrix-vector product by its standart way and our approach.

The *flops* needed to solve the linear system in equation 15 using the Cholesky factorization is:

$$f_{classical} = \frac{7}{3}N^3 + 6N^2 , \quad (69)$$

where  $N$  is the total number of observation points and also the size of estimated parameter vector  $\hat{\mathbf{p}}$ .

For the more efficient CGLS algorithm the estimative can be done in:

$$f_{cglsl} = 2N^2 + it(4N^2 + 12N) . \quad (70)$$

However, our approach reduces further to:

$$f_{ours} = \kappa 16N \log_2(4N) + 24N + it(\kappa 16N \log_2(4N) + 60N) , \quad (71)$$

where  $\kappa$  depends on the FFT algorithm. By default, in this work we will use  $\kappa = 5$  for the *radix-2* algorithm (Van Loan, 1992).

Figure 3 shows a comparative between the methods varying the number of observation points up to 1,000,000, where it is possible to observe a reduction of  $10^7$  orders of magnitude to estimate parameter vector  $\hat{\mathbf{p}}$  in relation to the non-iterative classical method and  $10^3$  orders of magnitude in relation to the standart CGLS algorithm using 50 iterations. A more detailed, step by step, flops count of the classical and CGLS algorithm can be found in Appendix A.

In figure 4 we show the time necessary to construct matrix  $\mathbf{A}$  (equation 12) and solve the linear system up to 10,000 points of observation. With this dataset the classical method

takes more than sixty-three seconds, the CGLS more than twelve seconds, while our method takes only half a second. The cpu used for this test was a intel core i7-7700HQ@2.8GHz.

In figure 5 a comparison between the time to complete the task to calculate the first column of the BCCB matrix embedded from the from  $\mathbf{A}$  (equation 12) by using only one equivalent source, i.e., calculating all six first column of the second derivatives matrices from  $\mathbf{H}$  (equation 10) and using four equivalent sources to calculate the four necessary columns from the non-symmetric matrix  $\mathbf{A}$  (equation 12). Although, very similar in time, with one source a small advantage can be observed as the number of data  $N$  increases and goes beyond  $N = 200,000$ . This test was done from  $N = 10,000$  to  $N = 700,000$  with increases of 5,625 observation points.

In Table 1 there is comparison between how much RAM memory is addressed to store the sensitivity matrix for each of the methods. The classical approach and the CGLS have to store the whole matrix  $\mathbf{A}$  (equation 12), this means that a dataset with for example  $N = 10,000$  observation points, the sensitivity matrix has  $N^2 = 100,000,000$  elements and takes approximately 763 Megabytes of memory (8 bytes per element). For our method, it is necessary to store the first six columns of each of the components from matrix  $\mathbf{H}$  (equation 10) embedded into the BCCB matrices. With the same dataset  $N = 10,000$  it needs 1.831 Megabytes. After completing the steps to store the eigenvalues of matrix  $\mathbf{C}$  (equation 63) it takes only 0.6104 Megabytes. Here, we are considering 16 bytes per element as the eigenvalues are complex numbers resulting from the 2D FFT. For a bigger dataset as  $N = 1,000,000$  the amount of RAM necessary goes to 7,629,395, 183.096 and 61.035 Megabytes, respectively, showing the necessity to find improved and efficient methods for the equivalent layer technique as the one presented in this work. We remember that throughout our work we are always considering  $N = M$ .

## APPLICATION TO SYNTHETIC DATA

The synthetic data application of the fast equivalent layer for magnetic data was conducted on a regular grid of  $80 \times 80$  points, totaling  $N = 6,400$  observation points. Three bodies were modeled: two prisms and a sphere with inclination, declination and intensity of  $0^\circ$  and  $45^\circ$  and  $2\sqrt{2}$  A/m, respectively. The main field has inclination and declination of  $10^\circ$  and  $37^\circ$ , respectively. Figure 6a shows the synthetic data created for this test.

Using a classical linear inversion method (equation 15) a predicted data was estimated in figure 7a. The residuals between the observed (6b) and the predicted data (7a), with mean 0.3712 nT and standart deviation of 0.2798 nT is shown in figure 7b. This process took 17.10 seconds.

Using the CGLS method with the fast BTTB matrix-vector product a predicted data was estimated in figure 8a. The residuals between the observed (6b) and the predicted data (8a), with mean 0.5150 nT and standart deviation of 0.4363 nT is shown in figure 8b. This process took 0.18 seconds.

In figure 9 we have the convergence analysis of the CGLS method to estimate the equivalent sources parameter vector  $\mathbf{d}(\hat{\mathbf{p}})$  used for this synthetic test. The squared euclidian norm of residuals decreases as expected, with good results at 50 iterations, stabilizing afterwards. This result shows that it is not necessary to run the conjugate gradient least square method at  $N$  iterations to get a theoretically exactly solution (which in practice would never occur due to roundoff errors), as this could be very demanding to process even with a small layer with  $N = 6,400$  equivalent sources. Setting a minimum tolerance of the residuals is a good option to carry out this algorithm efficiently and still obtaining very good results. Another possibility is to set an invariance to the euclidian norm of residuals

between iterations, which would increase algorithm runtime, but with smaller residuals. We chose the first option, as we achieve satisfactory results.

### Tests with irregular grids

As shown in theory, a regular grid of observation points is needed to arise the BTTB matrix. In this section, we show the results when this algorithm is used directly into irregular grids of  $N = 5\,000$  observation points. First, we set up a regular grid of  $100 \times 50$  observation points in the  $x$ - and  $y$ -directions with a grid spacing of  $\Delta x$  of 101.01 m along the  $x$ -axis and  $\Delta y$  of 163.265 m along the  $y$ -axis. Next, the  $x$  and  $y$  coordinates of the observations were also contaminated with pseudorandom Gaussian noise with zero mean and standard deviations of 10%, 30% and 50% of the  $\Delta x$  and  $\Delta y$  spacing.

Figure 10a shows an irregular grid with standard deviations of 10% along both  $x$ - and  $y$ -direction of the observation points. Using the classical approach the residuals between the observed (10b) and the predicted data (11a) has mean 0.3628 nT, standard deviation of 0.2727 nT and is shown in figure 11b. Using the new approach of this work the residuals between the observed (10b) and the predicted data (12a) has mean 0.6024 nT, standard deviation of 0.4998 nT and is shown in figure 12b. In figure 13 we have the convergence analysis of the CGLS method to estimate the equivalent sources used for this synthetic test. The squared euclidian norm decreases as expected, with good results at 50 iterations, stabilizing afterwards.

Figure 14a shows an irregular grid with standard deviations of 20% along both  $x$ - and  $y$ -direction of the observation points. Using the classical approach the residuals between the observed (14b) and the predicted data (15a) has mean 0.3630 nT, standard deviation of

0.2731 nT and is shown in figure 15b. Using the new approach of this work the residuals between the observed (14b) and the predicted data (16a) has mean 0.7147 nT, standart deviation of 0.5622 nT and is shown in figure 16b. In figure 17 we have the convergence analysis of the CGLS method to estimate the equivalent sources used for this synthetic test. The squared euclidian norm decreases as expected and stabilizing afterwards.

Figure 18a shows an irregular grid with standart deviations of 30% along both  $x$ - and  $y$ -direction of the observation points. Using the classical approach the residuals between the observed (18b) and the predicted data (19a) has mean 0.3634 nT, standart deviation of 0.2735 nT and is shown in figure 19b. Using the new approach of this work the residuals between the observed (18b) and the predicted data (20a) has mean 0.9788 nT, standart deviation of 0.7462 nT and is shown in figure 20b. In figure 21 we have the convergence analysis of the CGLS method to estimate the equivalent sources used for this synthetic test. The squared euclidian norm decreases as expected in the begining, but starts increasing and not converging afterwards.

This results show that, when this approach is used in irregular grids, there is a limit of how much deviation the observation points can have before it starts to produce errors in predicted data. This is confirmed with the convergence analysis, when the irregularity is too large, the linear system stops converging.

Another set of tests were also made with the same previous grid configuration, but now with deviations in the  $z$ -direction, i.e., the observation points were no longer in a plane. In the previous tests, the total-field anomaly was computed at 900 m height. The  $z$ coordinate of the observations were contaminated with pseudorandom Gaussian noise with zero mean and standard deviations of 5%, 10%, and 20% of the 900 height.

Figure 22a shows a regular grid of  $100 \times 50$  in the  $x$ - and  $y$ -directions located on an uneven surface of observations where the  $z$  coordinates were corrupted with a standard deviation of 5% of the height. Using the classical approach the residuals between the observed (22b) and the predicted data (23a) has mean 0.3712 nT, standart deviation of 0.2870 nT and is shown in figure 23b. Using the new approach of this work the residuals between the observed (22b) and the predicted data (24a) has mean 0.9542 nT, standart deviation of 0.8943 nT and is shown in figure 24b. In figure 25 we have the convergence analysis of the CGLS method to estimate the equivalent sources used for this synthetic test. The squared euclidian norm decreases as expected, with good results at 50 iterations, stabilizing afterwards.

Figure 26a shows a regular grid of  $100 \times 50$  in the  $x$ - and  $y$ -directions located on an uneven surface of observations where the  $z$  coordinates were corrupted with a standard deviation of 10% of the height. Using the classical approach the residuals between the observed (26b) and the predicted data (27a) has mean 0.3865 nT, standart deviation of 0.3216 nT and is shown in figure 27b. Using the new approach of this work the residuals between the observed (26b) and the predicted data (28a) has mean 1.6105 nT, standart deviation of 1.6231 nT and is shown in figure 28b. In figure 29 we have the convergence analysis of the CGLS method to estimate the equivalent sources used for this synthetic test. The squared euclidian norm decreases as expected, with good results at 50 iterations, stabilizing afterwards.

Figure 30a shows a regular grid of  $100 \times 50$  in the  $x$ - and  $y$ -directions located on an uneven surface of observations where the  $z$  coordinates were corrupted with a standard deviation of 20% of the height. Using the classical approach the residuals between the observed (30b) and the predicted data (31a) has mean 0.4155 nT, standart deviation of 0.4005 nT and is shown in figure 31b. Using the new approach of this work the residuals

between the observed (30b) and the predicted data (32a) has mean 6.6220 nT, standart deviation of 5.901 nT and is shown in figure 32b. In figure 33 we have the convergence analysis of the CGLS method to estimate the equivalent sources used for this synthetic test. The squared euclidian norm decreases slower than previous tests and starts increasing afterwards showing that the convergence is not possible.

Once again, we observe that while the classical linear inversion method can predict the data even with high irregularities in the observation points grid, the method presented in this work stars to create errors in the estimative. Through the convergence graphs it is possible to see the increase of the squared euclidian norm of the residuals, but the sensitivity to uncertainties in the  $z$  coordinates of the observations is higher than the the sensitivity to uncertainties in the  $x$  and  $y$  coordinates of the observations. With an average of 20% of deviation in the  $z$ -*direction* the system stopped converging while only at an average deviation of 30% in the  $x$ -*direction* and 30% in the  $y$ -*direction* that the same convergence problem occured.

## APPLICATION TO FIELD DATA

The field data application was made with the aeromagnetic data of Carajás, Pará, Brazil, provided by the CPRM. The total number of data is 7,706,153. For this case we gridded the data to  $500 \times 500 = 2,500,000$  observation points, which means that storing the full sensitivity matrix would be necessary 45.47 Terabytes of RAM. However, taking advantage that the second derivatives of equation 6 are symmetric or skew-symmetric matrices, it is possible to reconstruct the whole sensitivity matrix storing only the first column of each component of equation 10, thus, using only 114.44 Megabytes.

To achieve high efficiency in property estimative of the equivalent sources, the method CGLS for inversion was used, combined with a fast matrix-vector product, only possible because of the Block-Toeplitz Toeplitz-Block(BTTB) structure of the sensitivity matrix. This fast matrix-vector product was also used for data processing (upward continuation) in a very efficient way.

As this area is very large different values of the magnetic main field can be considered. For this test it was considered an approximated mid location of the area (latitude  $-6.5^\circ$  and longitude  $-50.75^\circ$ ) where the declination is  $-19.86^\circ$  for the IGRF model in 1st january, 2014. The inclination was calculated considering the Geocentric axial dipole model ( $\tan I = 2 \times \tan \lambda$ ) and is equal to  $12.84^\circ$ . As the source magnetization is unknown, inclination and declination equals to the main field is being used.

Figure 34 shows the observed magnetic field data of the area. Using a equivalent layer at 300 meters above the ground the predicted data and its residual are shown in figure 35. The mean of  $2.4566 \times 10^{-6}$  nT and the standart deviation of  $1.9787 \times 10^{-6}$  nT of the residual shows the good result of physical property estimative. It was used 50 iterations of

the CGLS method taking 15.5 seconds with a Intel core i7 7700HQ@2.8GHz processor.

The convergence analysis is shown in figure 36

In figure 37 the upward continuation transformation was made at 5000 meters and took 0.49 seconds.

## CONCLUSIONS

In this work, we were able to develop a fast equivalent layer technique for processing magnetic data with the method of Conjugate Gradient Least Square using the convolutional equivalent layer theory to obtain results of performance more than four orders of magnitude less than the classical equivalent layer. The sensitivity matrix of the magnetic equivalent layer carries the structure of BTTB matrices, which means a very low computational cost matrix-vector product and also the possibility to store only the first column of the matrix BCCB. In this work we propose a method to calculate the first six columns of the second derivatives matrices to embed them into BCCB and then finally arrive in what would be the first column of the BCCB matrix embedded from the sensitivity matrix.

Synthetic tests showed similar results estimating the physical property using a classical approach to solve a linear system and our method using the CGLS combined with the BTTB matrix-vector product. The difference in time, however, is noticeable: 2.04 seconds using the classical approach and 0.083 seconds using our approach. This difference was obtained with a mid-size mesh of  $80 \times 80$  points, greater results can be obtained if more observation points are used.

Real data test were also conducted in the region of Carajás, Pará, Brazil. With a regular grid of 2,500,000 observation points, store the full sensitivity matrix it would be necessary 45.47 Terabytes of RAM. However, taking advantage symmetric or skew-symmetric matrices structures, it is possible to reconstruct the whole sensitivity matrix using only 114.44 Megabytes. Using 50 iterations of the CGLS method took 15.5 seconds and very good results of property estimative were obtained. Also the upward continuation transformation was successfull with good results and taking only 0.49 seconds.

## **ACKNOWLEDGEMENTS**

Diego Takahashi was supported by a Phd scholarship from CAPES. Valéria C.F. Barbosa was supported by fellowships from CNPq (grant 307135/2014-4) and FAPERJ (grant 26/202.582/2019). Vanderlei C. Oliveira Jr. was supported by fellowships from CNPq (grant 308945/2017-4) and FAPERJ (grant E-26/202.729/2018). The authors thank the Geological Survey of Brazil (CPRM) for providing the field data.

## APPENDIX A

### FLOPS COMPUTATIONS

#### Classical flops count

The flops count of the classical approach to solve the linear system (equation 15) using the Cholesky factorization is given by equation 69. The step-by-step count follows:

- (1)  $\mathbf{A}^\top \mathbf{A}$ :  $2N^3$  (one matrix-matrix product).
- (2)  $\mathbf{A}^\top \mathbf{A}$ :  $\frac{1}{3}N^3$  (one Cholesky factorization  $\mathbf{C}_f$ ).
- (3)  $\mathbf{A}^\top \mathbf{d}^o$ :  $2N^2$  (one matrix-vector product).
- (4)  $\mathbf{C}_f(\mathbf{A}^\top \mathbf{d}^o)$ :  $2N^2$  (one matrix-vector product).
- (5)  $\mathbf{C}_f^\top (\mathbf{C}_f \mathbf{A}^\top \mathbf{d}^o)$ :  $2N^2$  (one matrix-vector product).

Summing all calculations:

$$f_{classical} = \frac{7}{3}N^3 + 6N^2, \quad (A-1)$$

#### CGLS flops count

The flops count of CGLS algorithm 1 can be summarized as:

Out of the loop:

- (1)  $\mathbf{A}^\top \mathbf{s}$ :  $2N^2$  (one matrix-vector product).

Inside the loop:

- (1)  $\frac{\mathbf{r}^{(it)\top} \mathbf{r}^{(it)}}{\mathbf{r}^{(it-1)\top} \mathbf{r}^{(it-1)}}$ :  $4N$  (two vector-vector products).
- (2)  $\mathbf{r}^{it} - \alpha_{it} \beta_{it} \mathbf{c}^{(it-1)}$ :  $2N$  (one scalar-vector product and one vector subtraction).
- (3)  $\frac{\|\mathbf{r}^{(it)}\|_2^2}{(\mathbf{c}^{(it)\top} \mathbf{A}^\top)(\mathbf{A} \mathbf{c}^{(it)})}$ :  $2N^2 + 2N$  (one matrix-vector and one vector-vector product).
- (4)  $\hat{\mathbf{p}}^{it} - \alpha_{it} \mathbf{c}^{(it)}$ :  $2N$  (one vector subtraction).
- (5)  $\mathbf{s}^{it} - \alpha_{it} \mathbf{A} \mathbf{c}^{(it)}$ :  $2N$  (one vector subtraction, the matrix-vector product was calculated in step 3).
- (6)  $\mathbf{A}^\top \mathbf{s}^{(it+1)}$ :  $2N^2$  (one matrix-vector product).

The result of all flops count leads to:

$$f_{cgls} = 2N^2 + it(4N^2 + 12N). \quad (\text{A-2})$$

### Our modified CGLS flops count

All the flops count presented in previous section for the CGLS remains, only substituting the out of the loop matrix-vector product in step 1 and the two matrix-vector products inside the loop in steps 3 and 6. The computations necessary to carry the matrix-vector used in this work are given by:

- (1)  $\mathbf{L}$ :  $\kappa 4N \log_2(4N)$  (one 2D FFT for the eigenvalues calculation of the sensitivity matrix  $\mathbf{A}$  or the transposed sensitivity matrix  $\mathbf{A}^\top$ ).
- (2)  $\mathbf{F}_{2Q} \mathbf{V} \mathbf{F}_{2P}$ :  $\kappa 4N \log_2(4N)$  (one 2D FFT).
- (3)  $\mathbf{L} \circ (\mathbf{F}_{2Q} \mathbf{V} \mathbf{F}_{2P})$ :  $24N$  (one complex Hadamard matrix multiplication).

(4)  $\mathbf{F}_{2Q}^* [\mathbf{L} \circ (\mathbf{F}_{2Q} \mathbf{V} \mathbf{F}_{2P})] \mathbf{F}_{2P}^*$ :  $\kappa 4N \log_2(4N)$  (one inverse 2D FFT).

Matrix-vector product total:  $\kappa 12N \log_2(4N) + 24N$ .

As matrix  $\mathbf{A}$  (equation 12) and its transposed never changes, it is not necessary to calculate the eigenvalues inside the loop at each iteration, we are considering that both are calculated out of the loop. Inside the loop, steps 2 to 4 are repeated two times per iteration. Substituting this result into the CGLS flops count (equation A-2) leads to:

$$f_{ours} = \kappa 16N \log_2(4N) + 24N + it(\kappa 16N \log_2(4N) + 60N). \quad (\text{A-3})$$

## REFERENCES

- Aster, R. C., B. Borchers, and C. H. Thurber, 2018, Parameter estimation and inverse problems: Elsevier.
- Blakely, R. J., 1996, Potential theory in gravity and magnetic applications, 1 ed.: Cambridge University Press.
- Chan, R. H.-F., and X.-Q. Jin, 2007, An introduction to iterative Toeplitz solvers: SIAM, 5.
- Dampney, C. N. G., 1969, The equivalent source technique: Geophysics, **34**, no. 1, 39–53.
- Emilia, D. A., 1973, Equivalent sources used as an analytic base for processing total magnetic field profiles: Geophysics, **38**, no. 2, 339–348.
- Golub, G. H., and C. F. V. Loan, 2013, Matrix computations (johns hopkins studies in the mathematical sciences), 4 ed.: Johns Hopkins University Press.
- Hogue, J. D., R. A. Renaut, and S. Vatankhah, 2020, A tutorial and open source software for the efficient evaluation of gravity and magnetic kernels: Computers & Geosciences, **144**, 104575.
- Leão, J. W. D., and J. B. C. Silva, 1989, Discrete linear transformations of potential field data: Geophysics, **54**, no. 4, 497–507.
- Levinson, N., 1946, The wiener (root mean square) error criterion in filter design and prediction: Journal of Mathematics and Physics, **25**, no. 1-4, 261–278.
- Li, Y., M. Nabighian, and D. W. Oldenburg, 2014, Using an equivalent source with positivity for low-latitude reduction to the pole without striation: Geophysics, **79**, J81–J90.
- Li, Y., and D. W. Oldenburg, 2010, Rapid construction of equivalent sources using wavelets: Geophysics, **75**, no. 3, L51–L59.
- Mendonça, C. A., 2020, Subspace method for solving large-scale equivalent layer and density

mapping problems: *Geophysics*, **85**, G57–G68.

Mendonça, C. A., and J. B. C. Silva, 1994, The equivalent data concept applied to the interpolation of potential field data: *Geophysics*, **59**, no. 5, 722–732.

Oliveira Jr., V. C., V. C. F. Barbosa, and L. Uieda, 2013, Polynomial equivalent layer: *Geophysics*, **78**, no. 1, G1–G13.

Renaut, R. A., J. D. Hogue, S. Vatankhah, and S. Liu, 2020, A fast methodology for large-scale focusing inversion of gravity and magnetic data using the structured model matrix and the 2-d fast fourier transform: *Geophysical Journal International*, **223**, 1378–1397.

Siqueira, F. C., V. C. Oliveira Jr, and V. C. Barbosa, 2017, Fast iterative equivalent-layer technique for gravity data processing: A method grounded on excess mass constraint: *Geophysics*, **82**, no. 4, G57–G69.

Takahashi, D., V. C. Oliveira Jr, and V. C. Barbosa, 2020, Convolutional equivalent layer for gravity data processing: *Geophysics*, **85**, G129–G141.

Van Loan, C., 1992, Computational frameworks for the Fast Fourier Transform: SIAM.

Zhang, Y., and Y. S. Wong, 2015, BTTB-based numerical schemes for three-dimensional gravity field inversion: *Geophysical Journal International*, **203**, no. 1, 243–256.

Zhang, Y., Y. S. Wong, and Y. Lin, 2016, BTTB–RRCG method for downward continuation of potential field data: *Journal of Applied Geophysics*, **126**, 74–86.

## LIST OF TABLES

1 This table shows the RAM memory usage (in Megabytes) for storing the whole matrix **A** (equation 12), the sum of all six first columns of the BCCB matrices embedded from the components of the matrix **H** from equation 10 (both need 8 bytes per element) and the matrix **L** containing the eigenvalues complex numbers (16 bytes per element) resulting from the diagonalization of matrix **C** (equation 63). Here we must consider that  $N$  observation points forms a  $N \times N$  matrix.

## LIST OF FIGURES

1 Schematic representation of an  $N_x \times N_y$  regular grid of points (black dots) defined by  $N_x = 4$  and  $N_y = 3$ . The grids are oriented along the (a)  $x$ -axis and (b)  $y$ -axis. The grid coordinates are  $x_k$  and  $y_k$ , where the  $k = 1, \dots, N_x$  and  $l = 1, \dots, N_y$  are called the grid indices. The insets show the grid indices  $k$  and  $l$ .

2 Representation of the four equivalent sources (black dots) needed to reconstruct the non-symmetric matrix  $\mathbf{A}$  (equation 12). Each of the equivalent sources are located in the corner of the simulated regular grid of  $M_x = 4$  and  $M_y = 3$  sources. The influence of these sources on each of the observation points (blue dots) in the regular grid of  $N_x = 4$  and  $N_y = 3$  will give the four columns necessary of matrix  $\mathbf{A}$ .

3 Number of flops necessary to estimate the parameter vector  $\hat{\mathbf{p}}$  using the non-iterative classical method (equation 69) the CGLS (equation 70) and our modified CGLS method (equation 71) with  $N^{it} = 50$ . The observation point  $N$  varied from 5,000 to 1,000,000. The radix-2 2D FFT algorithm was considered for our method, with  $\kappa = 5$ .

4 Comparison between the runtime of the equivalent-layer technique using the classical, the CGLS algorithm and our method. The values for the CGLS and our methods were obtained for  $N^{it} = 50$  iterations.

5 Comparison between the runtime to calculate the first column of the BCCB matrix embedded from  $\mathbf{A}$  (equation 12) using only one and using four equivalent sources. Although the time is very similar, with one source a small advantage can be observed as the number of data  $N$  increases. This test was done from  $N = 10,000$  to  $N = 700,000$  with increases of 5,625 observation points.

6 Observed synthetic magnetic field data. A regular grid of  $80 \times 80$  points was used, totaling  $N = 6,400$  observation points. Three bodies were modeled: two prisms and a

sphere with inclination, declination and intensity of  $0^\circ$  and  $45^\circ$  and  $2 \times \sqrt{2}$  A/m, respectively.

7 (a) Predicted data using a classical linear inversion method (equation 15). (b) Residuals between the observed (6) and the predicted data (panel a), with mean 0.3712 nT and standart deviation of 0.2798 nT. This process took 17.6 seconds.

8 (a) Predicted data using the CGLS method with the fast BTTB matrix-vector product. (b) Residuals between the observed (6) and the predicted data (panel a), with mean 0.5150 nT and standart deviation of 0.4363 nT. This process took 0.18 seconds.

9 Convergence analysis of the CGLS method for this synthetic application of the magnetic equivalent layer using the fast BTTB matrix-vector product.

10 (a) Synthetic magnetic field grid visualization. A irregular grid of  $100 \times 50$  points was used, totaling  $N = 5,000$  observation points. Standart deviations of 10% in the  $x$ -direction and 10% in the  $y$ -direction were applied. (b) Observed synthetic magnetic field data using this irregular grid in panel a. Three bodies were modeled: two prisms and a sphere with inclination, declination and intensity of  $0^\circ$  and  $45^\circ$  and  $2 \times \sqrt{2}$  A/m, respectively.

11 (a) Predicted data using a classical linear inversion method (equation 15) for the irregular grid in figure 10a. (b) Residuals between the observed (10b) and the predicted data (panel a), with mean 0.3628 nT and standart deviation of 0.2727 nT.

12 (a) Predicted data using the CGLS method with the fast BTTB matrix-vector product for for the irregular grid in figure 10a. (b) Residuals between the observed (10b) and the predicted data (panel a), with mean 0.6024 nT and standart deviation of 0.4998 nT.

13 Convergence analysis of the CGLS method for the synthetic application of the mag-

netic equivalent layer using an irregular grid with 10% of perturbation on the *x*-*direction* and *y*-*direction*.

14 (a) Synthetic magnetic field grid visualization. A irregular grid of  $100 \times 50$  points was used, totaling  $N = 5,000$  observation points. Standard deviations of 20% in the *x*-direction and 20% in the *y*-direction were applied. (b) Observed synthetic magnetic field data using this irregular grid in panel a. Three bodies were modeled: two prisms and a sphere with inclination, declination and intensity of  $0^\circ$  and  $45^\circ$  and  $2 \times \sqrt{2}$  A/m, respectively.

15 (a) Predicted data using a classical linear inversion method (equation 15) for the irregular grid in figure 14a. (b) Residuals between the observed (14b) and the predicted data (panel a), with mean 0.3630 nT and standard deviation of 0.2731 nT.

16 (a) Predicted data using the CGLS method with the fast BTTB matrix-vector product for the irregular grid in figure 14a. (b) Residuals between the observed (14b) and the predicted data (panel a), with mean 0.7147 nT and standard deviation of 0.5622 nT.

17 Convergence analysis of the CGLS method for the synthetic application of the magnetic equivalent layer using an irregular grid with 20% of perturbation on the *x*-*direction* and *y*-*direction*.

18 (a) Synthetic magnetic field grid visualization. A irregular grid of  $100 \times 50$  points was used, totaling  $N = 5,000$  observation points. Standard deviations of 30% in the *x*-direction and 30% in the *y*-direction were applied. (b) Observed synthetic magnetic field data using this irregular grid in panel a. Three bodies were modeled: two prisms and a sphere with inclination, declination and intensity of  $0^\circ$  and  $45^\circ$  and  $2 \times \sqrt{2}$  A/m, respectively.

19 (a) Predicted data using a classical linear inversion method (equation 15) for the irregular grid in figure 18a. (b) Residuals between the observed (18b) and the predicted data (panel a), with mean 0.3634 nT and standart deviation of 0.2735 nT.

20 (a) Predicted data using the CGLS method with the fast BTTB matrix-vector product for for the irregular grid in figure 18a. (b) Residuals between the observed (18b) and the predicted data (panel a), with mean 0.9788 nT and standart deviation of 0.7462 nT.

21 Convergence analysis of the CGLS method for the synthetic application of the magnetic equivalent layer using an irregular grid with 30% of pertubation on the *x*-direction and *y*-direction.

22 (a) Undulating surface where the total-field anomaly was computed. A irregular grid of  $100 \times 50$  points was used, totaling  $N = 5,000$  observation points. A standart deviation of 5% in the *z*-direction was applied. (b) Observed synthetic magnetic field data using this irregular grid in panel a. Three bodies were modeled: two prisms and a sphere with inclination, declination and intensity of  $0^\circ$  and  $45^\circ$  and  $2 \times \sqrt{2}$  A/m, respectively.

23 (a) Predicted data using a classical linear inversion method (equation 15) for the irregular grid in figure 22a. (b) Residuals between the observed (22b) and the predicted data (panel a), with mean 0.3712 nT and standart deviation of 0.2870 nT.

24 (a) Predicted data using the CGLS method with the fast BTTB matrix-vector product for for the irregular grid in figure 22a. (b) Residuals between the observed (22b) and the predicted data (panel a), with mean 0.9542 nT and standart deviation of 0.8943 nT.

25 Convergence analysis of the CGLS method for the synthetic application of the magnetic equivalent layer using an irregular grid with 5% of pertubation on the *z*-direction.

26 (a) Undulating surface where the total-field anomaly was computed. A irregular grid of  $100 \times 50$  points was used, totaling  $N = 5,000$  observation points. A standart deviation of 10% in the  $z$ -direction was applied. (b) Observed synthetic magnetic field data using this irregular grid in panel a. Three bodies were modeled: two prisms and a sphere with inclination, declination and intensity of  $0^\circ$  and  $45^\circ$  and  $2 \times \sqrt{2}$  A/m, respectively.

27 (a) Predicted data using a classical linear inversion method (equation 15) for the irregular grid in figure 26a. (b) Residuals between the observed (26b) and the predicted data (panel a), with mean 0.3865 nT and standart deviation of 0.3216 nT.

28 (a) Predicted data using the CGLS method with the fast BTTB matrix-vector product for for the irregular grid in figure 26a. (b) Residuals between the observed (26b) and the predicted data (panel a), with mean 1.6105 nT and standart deviation of 1.6231 nT.

29 Convergence analysis of the CGLS method for the synthetic application of the magnetic equivalent layer using an irregular grid with 10% of pertubation on the  $z$ -direction.

30 (a) Undulating surface where the total-field anomaly was computed. A irregular grid of  $100 \times 50$  points was used, totaling  $N = 5,000$  observation points. A standart deviation of 20% in the  $z$ -direction was applied. (b) Observed synthetic magnetic field data using this irregular grid in panel a. Three bodies were modeled: two prisms and a sphere with inclination, declination and intensity of  $0^\circ$  and  $45^\circ$  and  $2 \times \sqrt{2}$  A/m, respectively.

31 (a) Predicted data using a classical linear inversion method (equation 15) for the irregular grid in figure 30a. (b) Residuals between the observed (30b) and the predicted data (panel a), with mean 0.4155 nT and standart deviation of 0.4005 nT.

32 (a) Predicted data using the CGLS method with the fast BTTB matrix-vector

product for for the irregular grid in figure 30a. (b) Residuals between the observed (30b) and the predicted data (panel a), with mean  $6.6220 \text{ nT}$  and standart deviation of  $5.901 \text{ nT}$ .

33 Convergence analysis of the CGLS method for the synthetic application of the magnetic equivalent layer using an irregular grid with 20% of pertubation on the *z*-direction.

34 Observed magnetic field data of the Carajás, Brazil area. A regular grid of  $500 \times 500$  points was used, totaling  $N = 250, 000$  observation points.

35 (a) Predicted data using our method. (b) Residuals between the observed (34) and the predicted data (panel a), with mean  $2.4566 \times 10^{-7} \text{ nT}$  and standart deviation of  $1.9787 \times 10^{-6} \text{ nT}$ .

36 Convergence analysis of the CGLS method for the field data of Carajás, Brazil using the magnetic equivalent layer with a regular grid of  $500 \times 500$  points.

37 Upward continuation transformation of real data of Carajás, Brazil at 5000 meter. It was necessary 0.49 seconds to complete the process.

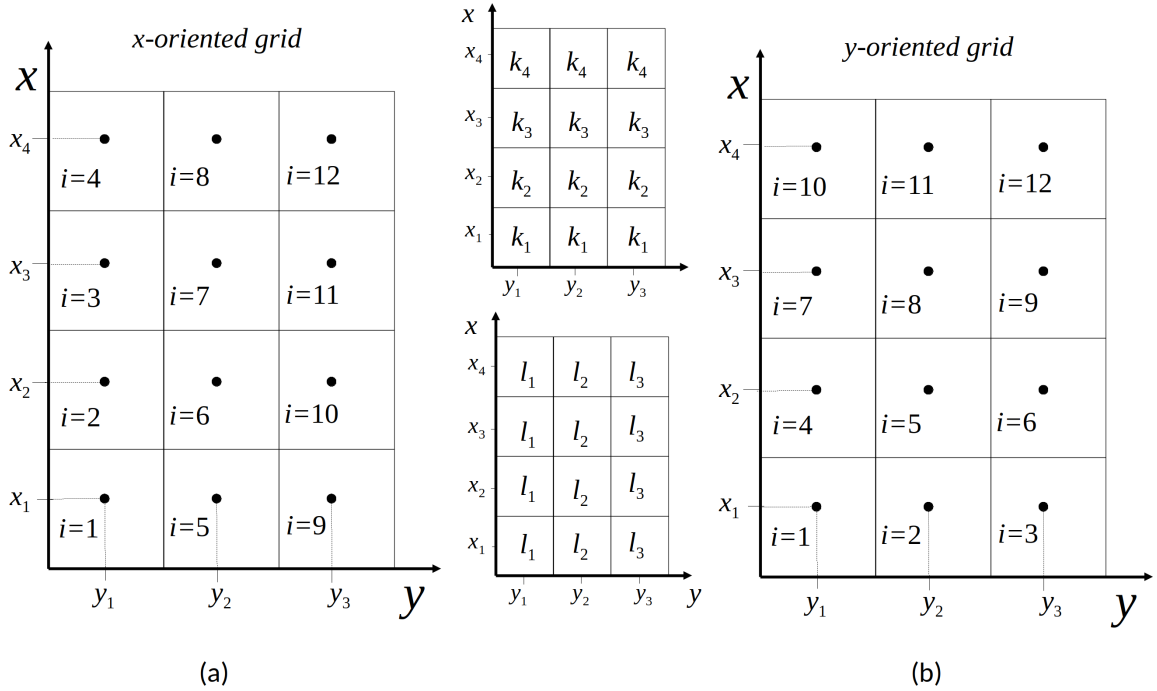


Figure 1: Schematic representation of an  $N_x \times N_y$  regular grid of points (black dots) defined by  $N_x = 4$  and  $N_y = 3$ . The grids are oriented along the (a)  $x$ -axis and (b)  $y$ -axis. The grid coordinates are  $x_k$  and  $y_l$ , where the  $k = 1, \dots, N_x$  and  $l = 1, \dots, N_y$  are called the grid indices. The insets show the grid indices  $k$  and  $l$ .

Takahashi, Oliveira Jr. & Barbosa – GEO-XXXX

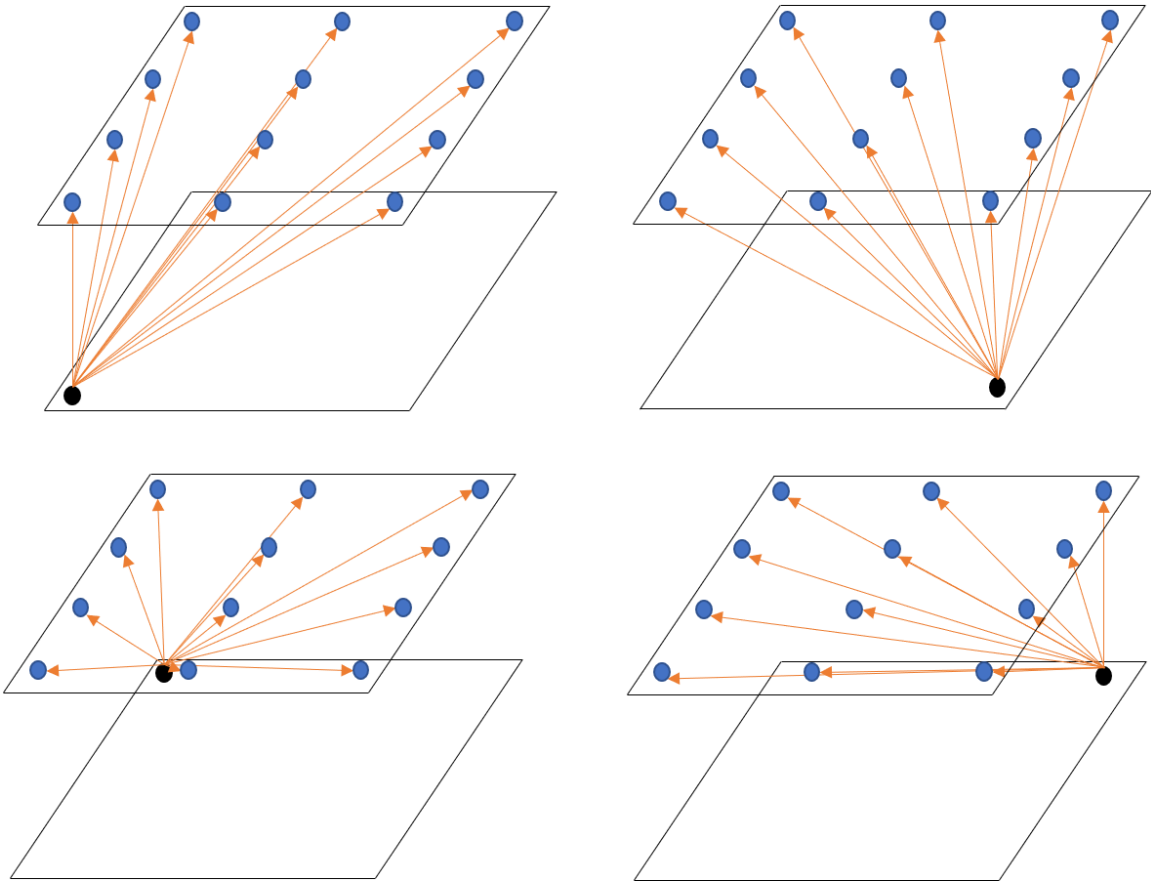


Figure 2: Representation of the four equivalent sources (black dots) needed to reconstruct the non-symmetric matrix  $\mathbf{A}$  (equation 12). Each of the equivalent sources are located in the corner of the simulated regular grid of  $M_x = 4$  and  $M_y = 3$  sources. The influence of these sources on each of the observation points (blue dots) in the regular grid of  $N_x = 4$  and  $N_y = 3$  will give the four columns necessary of matrix  $\mathbf{A}$ .

**Takahashi, Oliveira Jr. & Barbosa – GEO-XXXX**

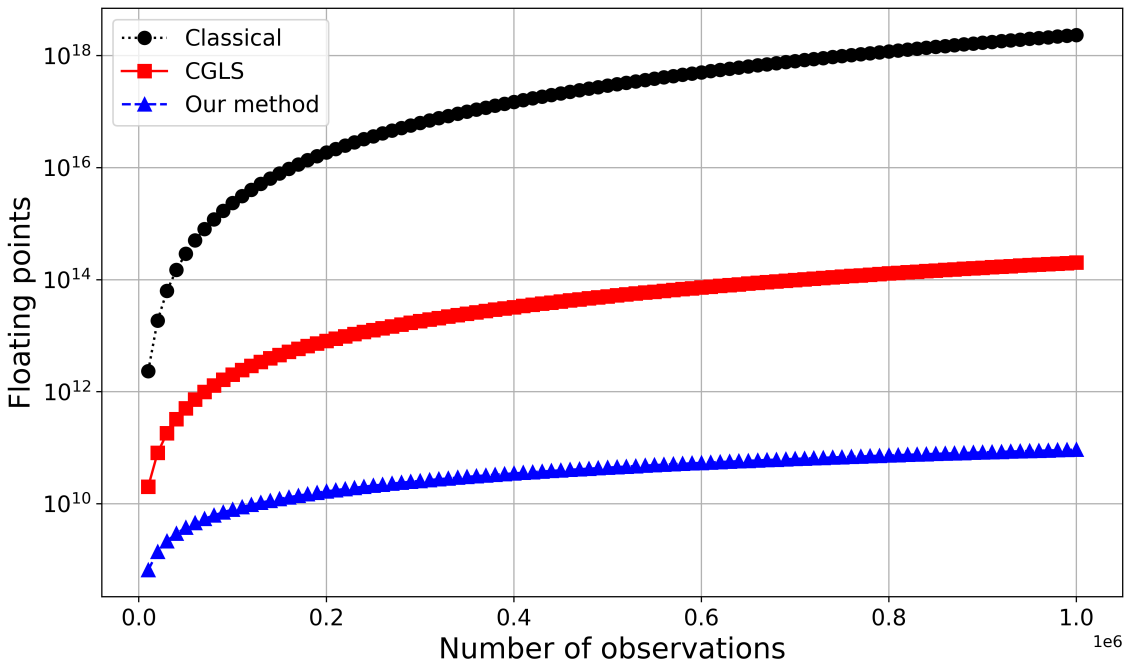


Figure 3: Number of flops necessary to estimate the parameter vector  $\hat{\mathbf{p}}$  using the non-iterative classical method (equation 69) the CGLS (equation 70) and our modified CGLS method (equation 71) with  $N^{it} = 50$ . The observation point  $N$  varied from 5,000 to 1,000,000. The radix-2 2D FFT algorithm was considered for our method, with  $\kappa = 5$ .

**Takahashi, Oliveira Jr. & Barbosa – GEO-XXXX**

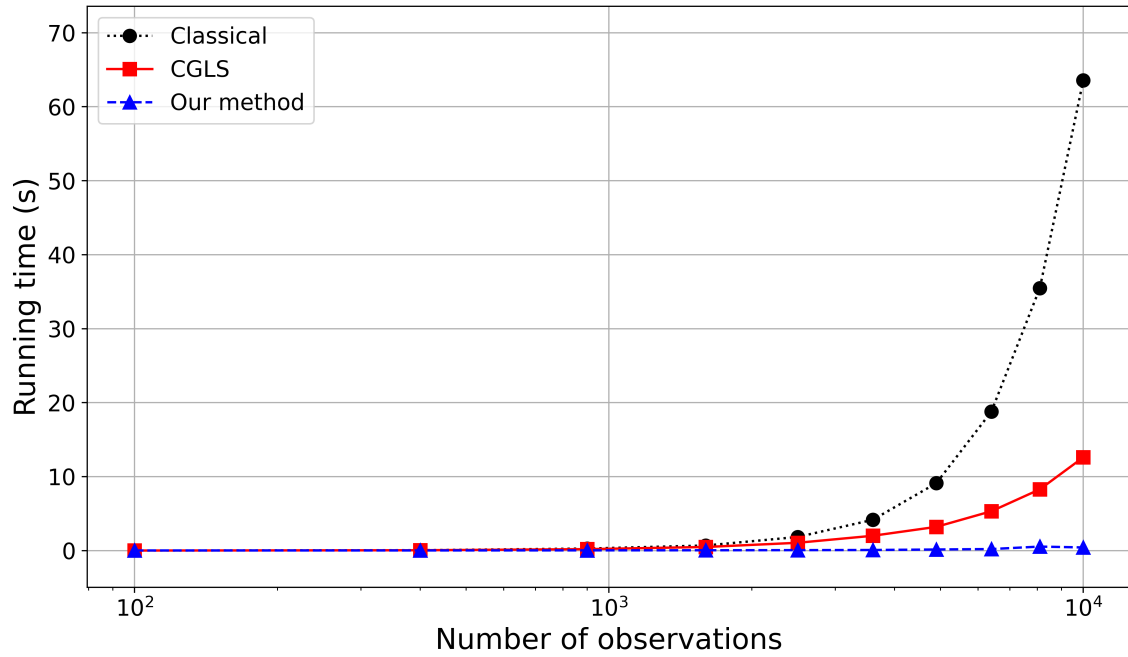


Figure 4: Comparison between the runtime of the equivalent-layer technique using the classical, the CGLS algorithm and our method. The values for the CGLS and our methods were obtained for  $N^{it} = 50$  iterations.

Takahashi, Oliveira Jr. & Barbosa – GEO-XXXX

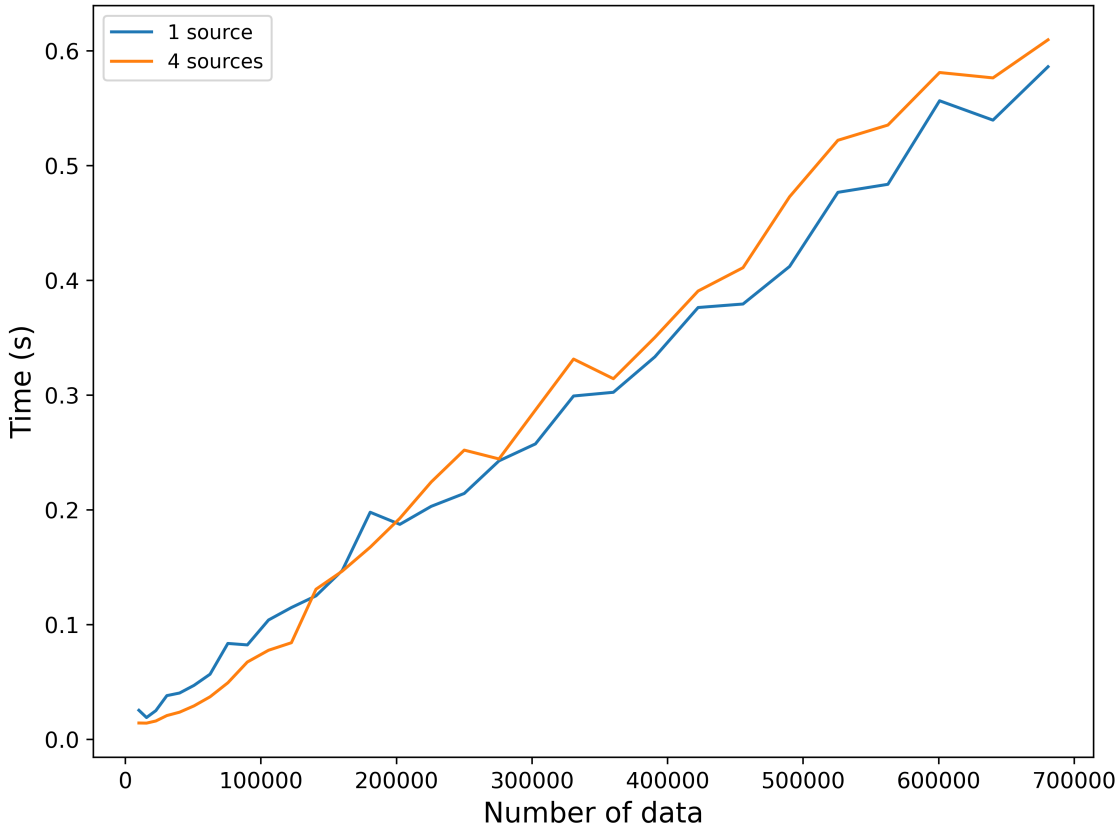


Figure 5: Comparison between the runtime to calculate the first column of the BCCB matrix embedded from  $\mathbf{A}$  (equation 12) using only one and using four equivalent sources. Although the time is very similar, with one source a small advantage can be observed as the number of data  $N$  increases. This test was done from  $N = 10,000$  to  $N = 700,000$  with increases of 5,625 observation points.

Takahashi, Oliveira Jr. & Barbosa – GEO-XXXX

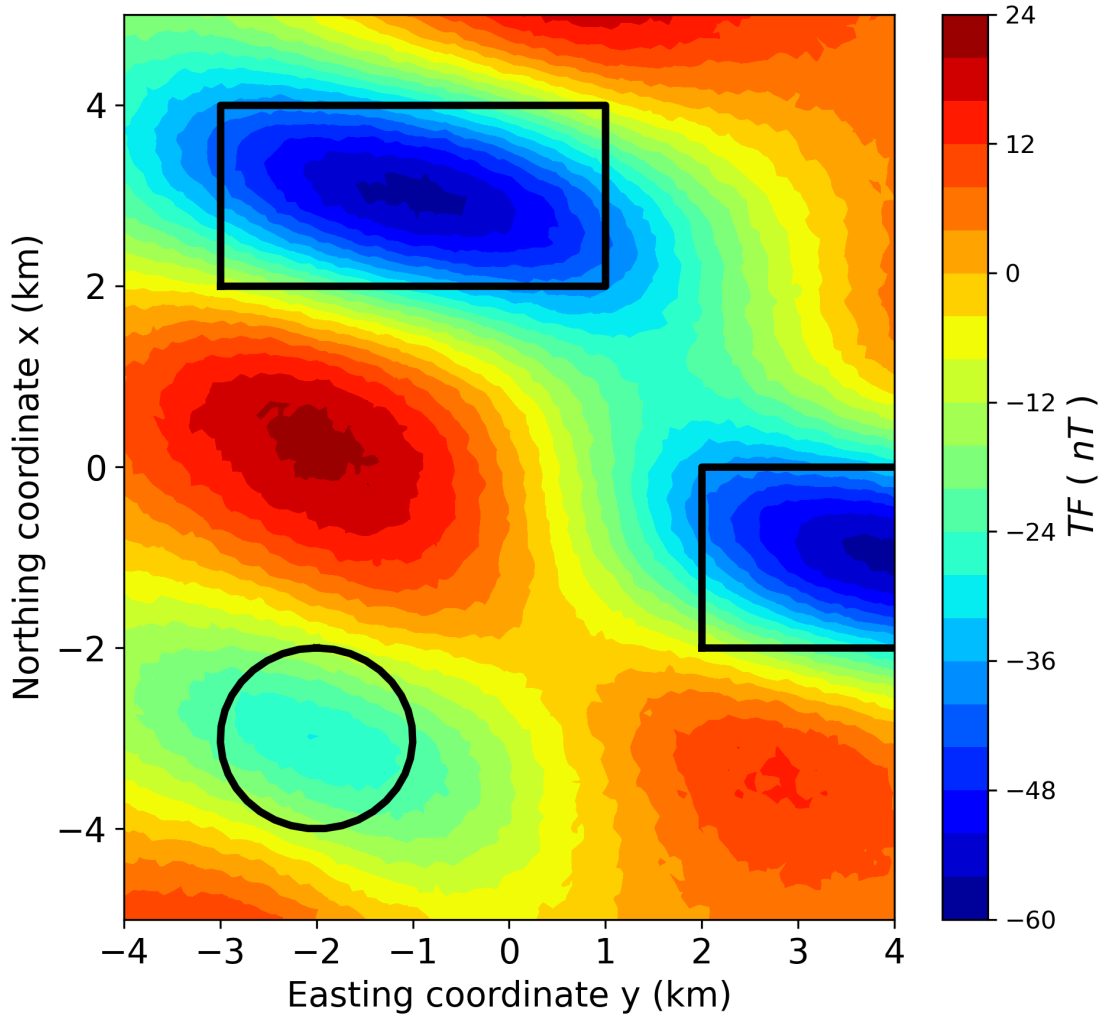


Figure 6: Observed synthetic magnetic field data. A regular grid of  $80 \times 80$  points was used, totaling  $N = 6,400$  observation points. Three bodies were modeled: two prisms and a sphere with inclination, declination and intensity of  $0^\circ$  and  $45^\circ$  and  $2 \times \sqrt{2}$  A/m, respectively.

Takahashi, Oliveira Jr. & Barbosa – GEO-XXXX

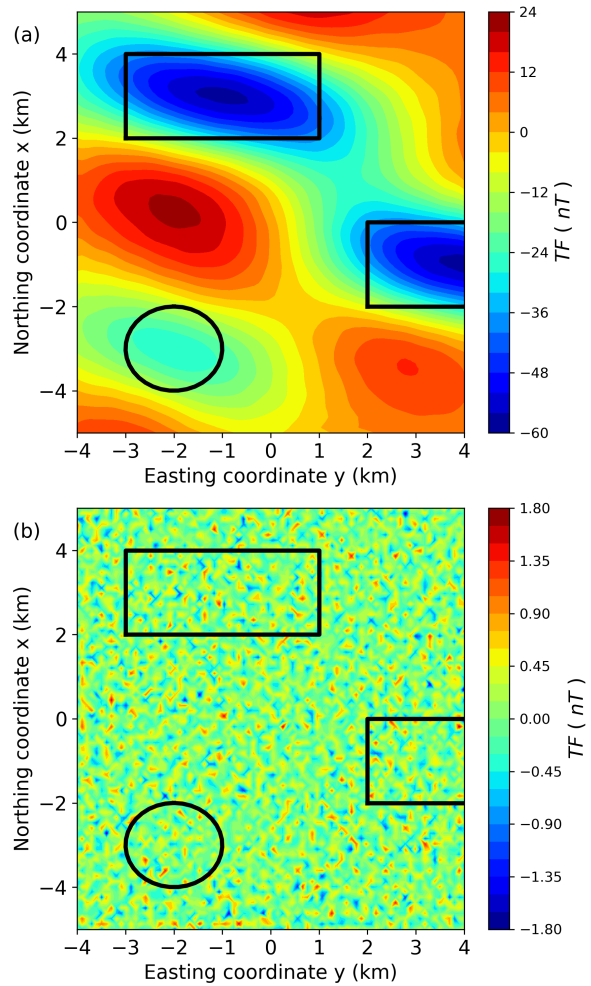


Figure 7: (a) Predicted data using a classical linear inversion method (equation 15). (b) Residuals between the observed (6) and the predicted data (panel a), with mean 0.3712 nT and standard deviation of 0.2798 nT. This process took 17.6 seconds.

Takahashi, Oliveira Jr. & Barbosa – GEO-XXXX

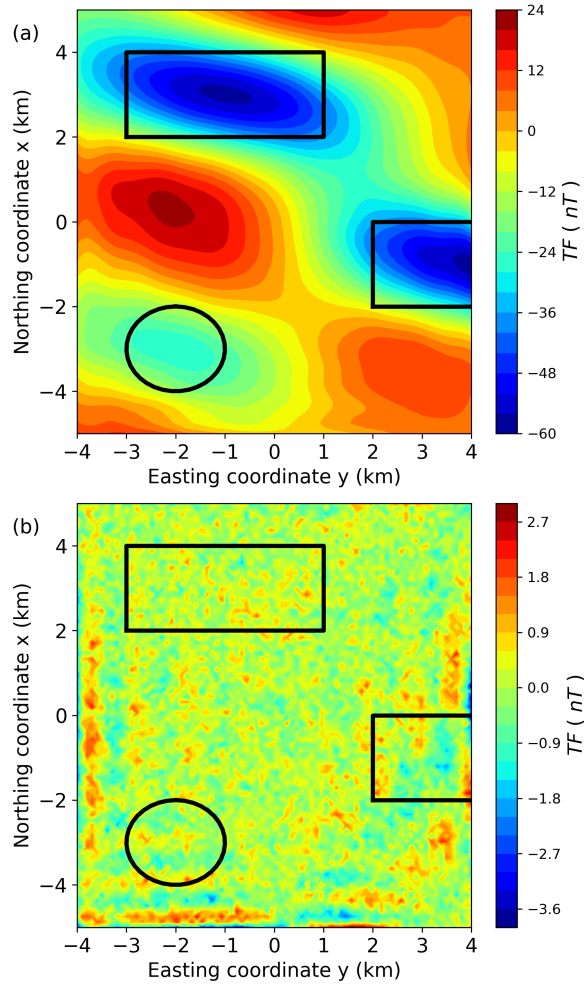


Figure 8: (a) Predicted data using the CGLS method with the fast BTTB matrix-vector product. (b) Residuals between the observed (6) and the predicted data (panel a), with mean 0.5150 nT and standart deviation of 0.4363 nT. This process took 0.18 seconds.

**Takahashi, Oliveira Jr. & Barbosa – GEO-XXXX**

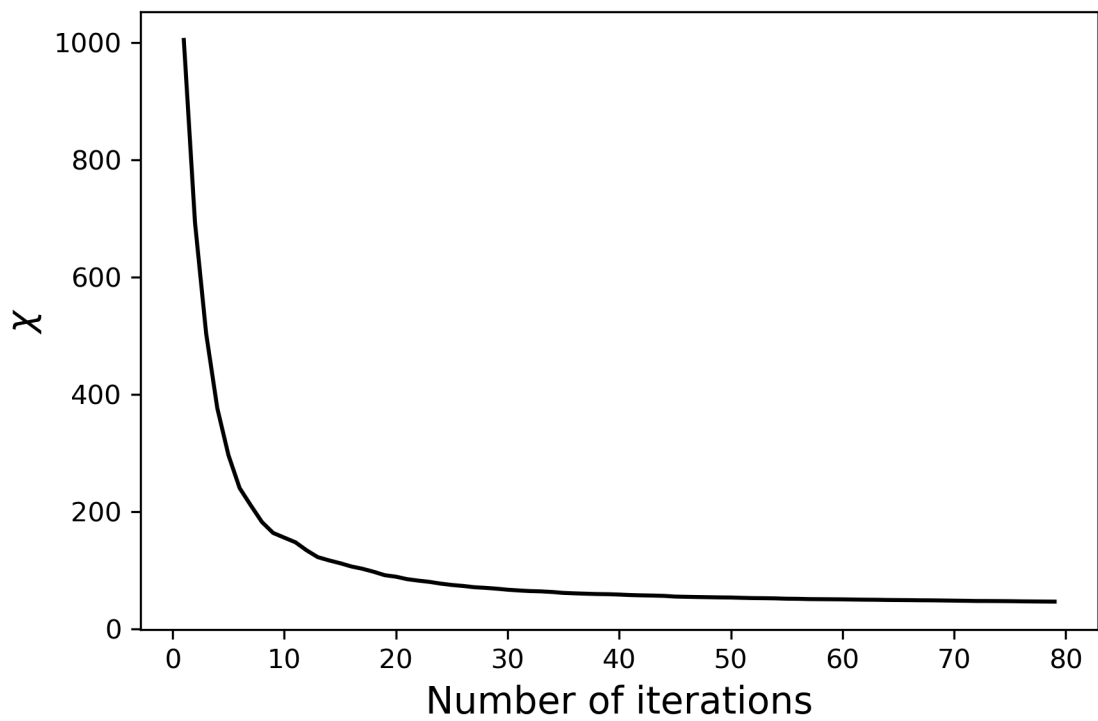


Figure 9: Convergence analysis of the CGLS method for this synthetic application of the magnetic equivalent layer using the fast BTTB matrix-vector product.

Takahashi, Oliveira Jr. & Barbosa – GEO-XXXX

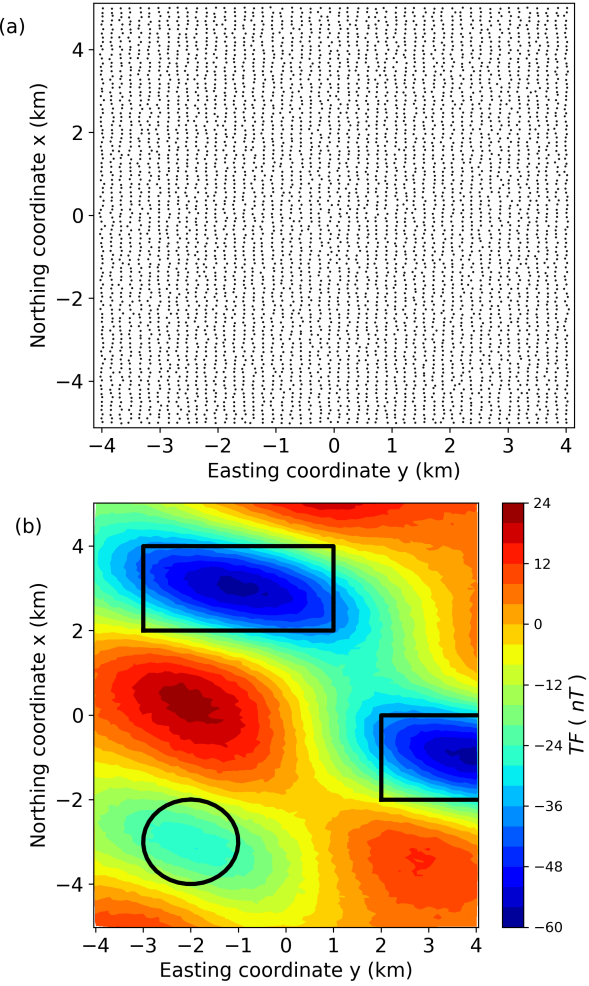


Figure 10: (a) Synthetic magnetic field grid visualization. A irregular grid of  $100 \times 50$  points was used, totaling  $N = 5,000$  observation points. Standard deviations of 10% in the  $x$ -direction and 10% in the  $y$ -direction were applied. (b) Observed synthetic magnetic field data using this irregular grid in panel a. Three bodies were modeled: two prisms and a sphere with inclination, declination and intensity of  $0^\circ$  and  $45^\circ$  and  $2 \times \sqrt{2}$  A/m, respectively.

**Takahashi, Oliveira Jr. & Barbosa – GEO-XXXX**

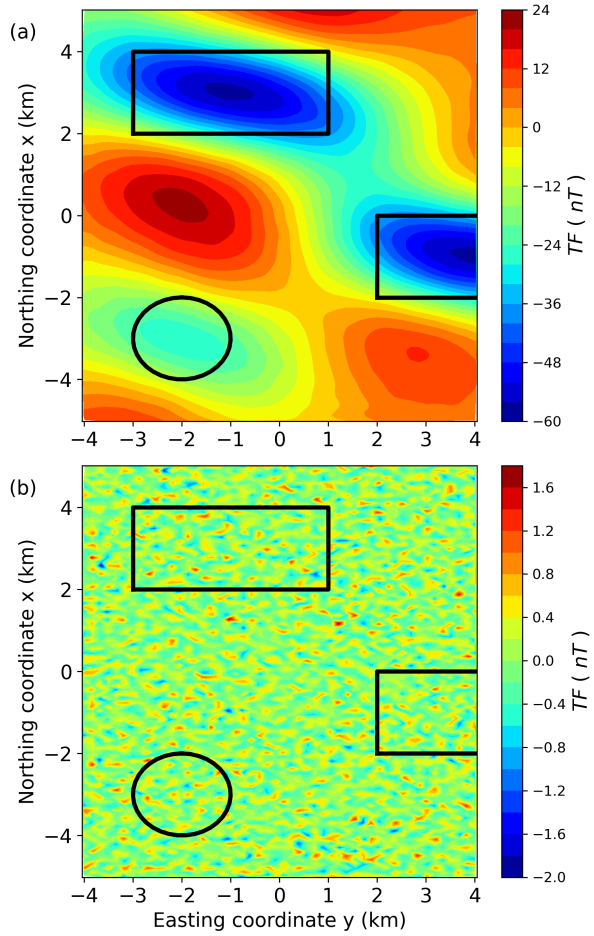


Figure 11: (a) Predicted data using a classical linear inversion method (equation 15) for the irregular grid in figure 10a. (b) Residuals between the observed (10b) and the predicted data (panel a), with mean 0.3628 nT and standart deviation of 0.2727 nT.

Takahashi, Oliveira Jr. & Barbosa – GEO-XXXX

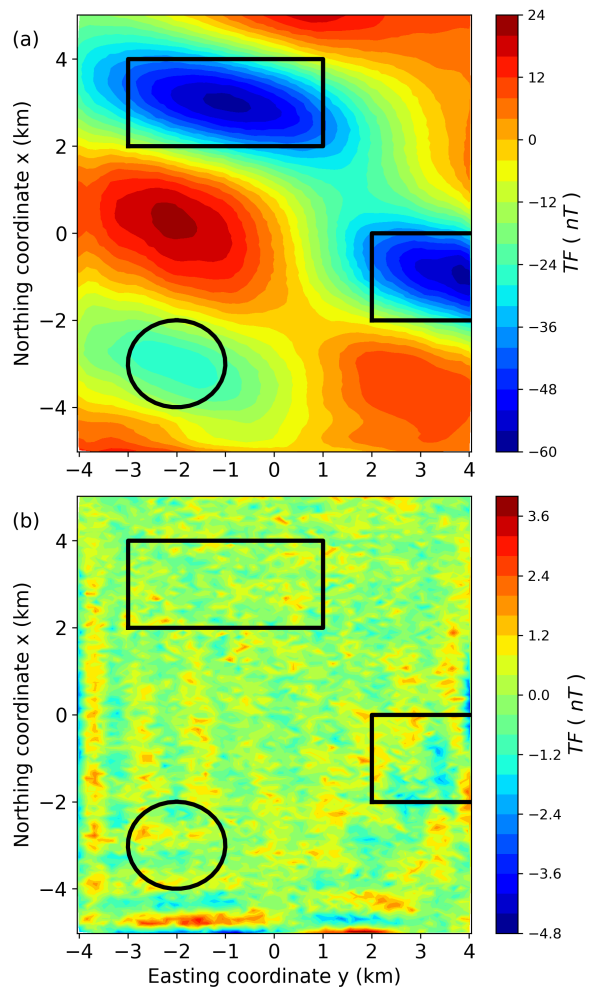


Figure 12: (a) Predicted data using the CGLS method with the fast BTTB matrix-vector product for the irregular grid in figure 10a. (b) Residuals between the observed (10b) and the predicted data (panel a), with mean 0.6024 nT and standard deviation of 0.4998 nT.

Takahashi, Oliveira Jr. & Barbosa – GEO-XXXX

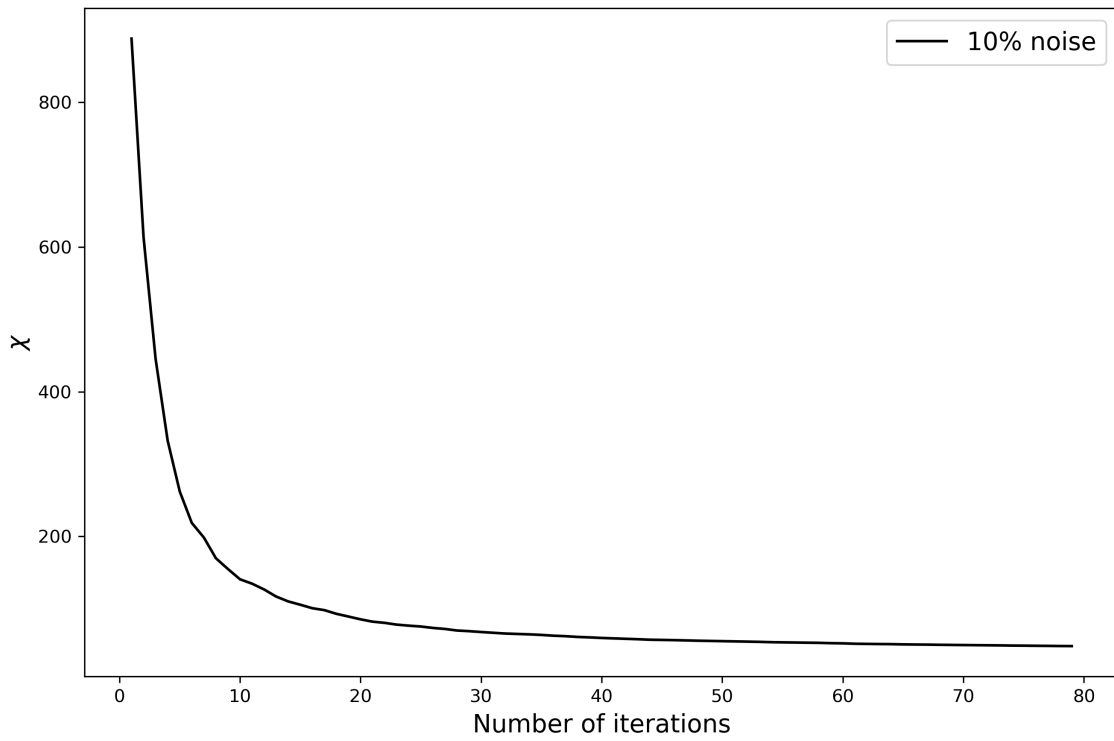


Figure 13: Convergence analysis of the CGLS method for the synthetic application of the magnetic equivalent layer using an irregular grid with 10% of perturbation on the *x-direction* and *y-direction*.

**Takahashi, Oliveira Jr. & Barbosa – GEO-XXXX**

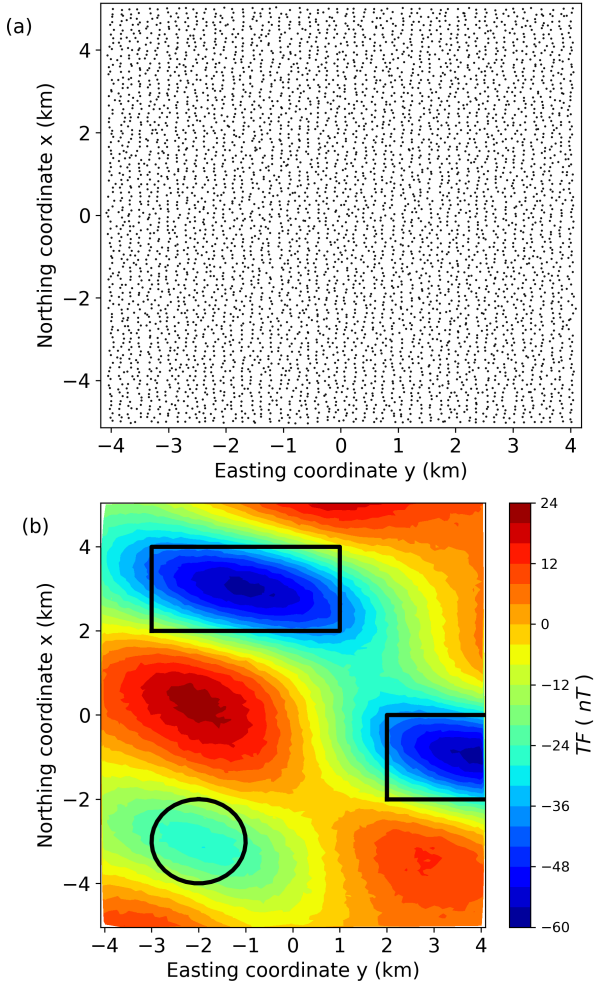


Figure 14: (a) Synthetic magnetic field grid visualization. A irregular grid of  $100 \times 50$  points was used, totaling  $N = 5,000$  observation points. Standart deviations of 20% in the  $x$ -direction and 20% in the  $y$ -direction were applied. (b) Observed synthetic magnetic field data using this irregular grid in panel a. Three bodies were modeled: two prisms and a sphere with inclination, declination and intensity of  $0^\circ$  and  $45^\circ$  and  $2 \times \sqrt{2}$  A/m, respectively.

**Takahashi, Oliveira Jr. & Barbosa – GEO-XXXX**

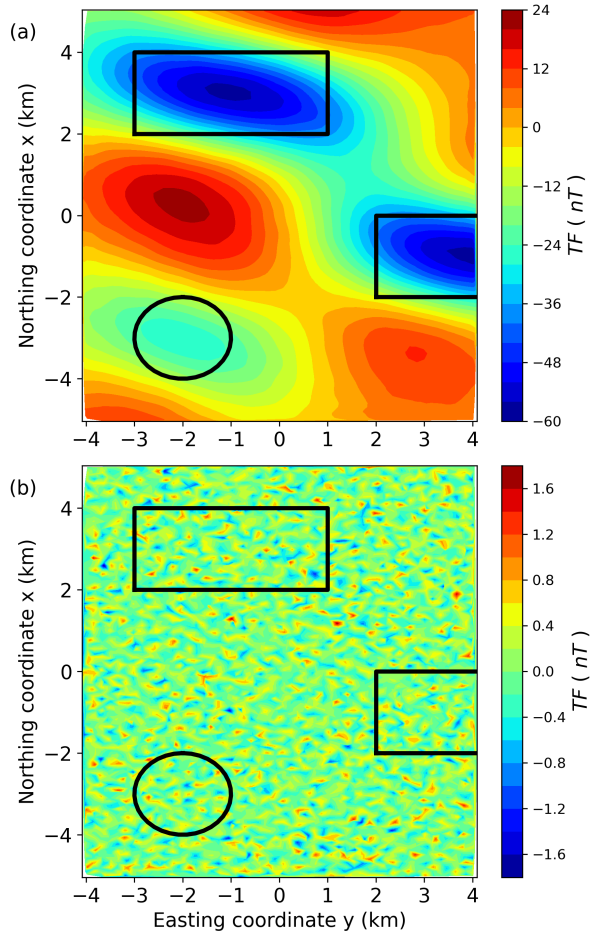


Figure 15: (a) Predicted data using a classical linear inversion method (equation 15) for the irregular grid in figure 14a. (b) Residuals between the observed (14b) and the predicted data (panel a), with mean 0.3630 nT and standart deviation of 0.2731 nT.

Takahashi, Oliveira Jr. & Barbosa – GEO-XXXX

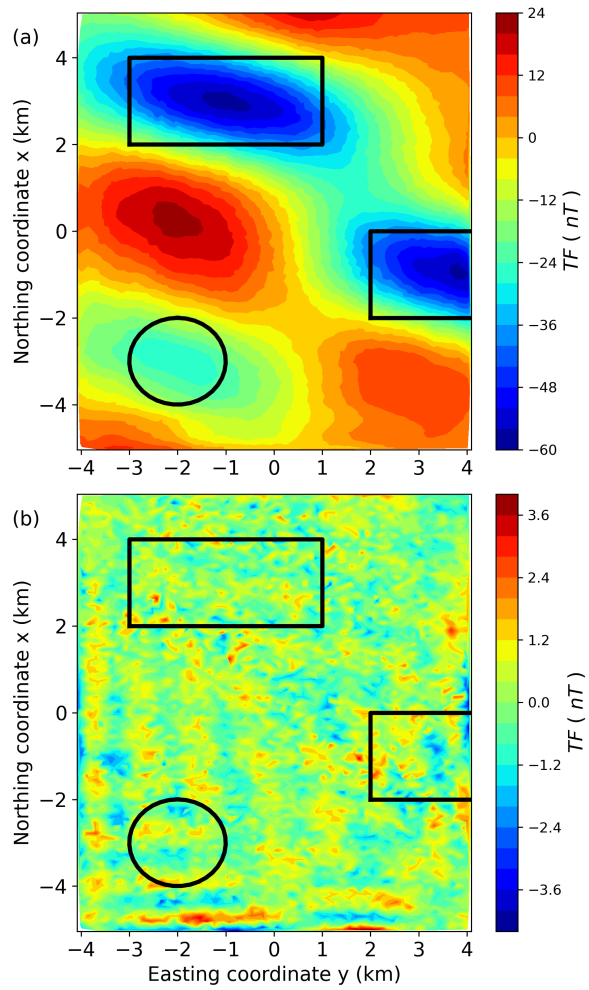


Figure 16: (a) Predicted data using the CGLS method with the fast BTTB matrix-vector product for the irregular grid in figure 14a. (b) Residuals between the observed (14b) and the predicted data (panel a), with mean 0.7147 nT and standard deviation of 0.5622 nT.

Takahashi, Oliveira Jr. & Barbosa – GEO-XXXX

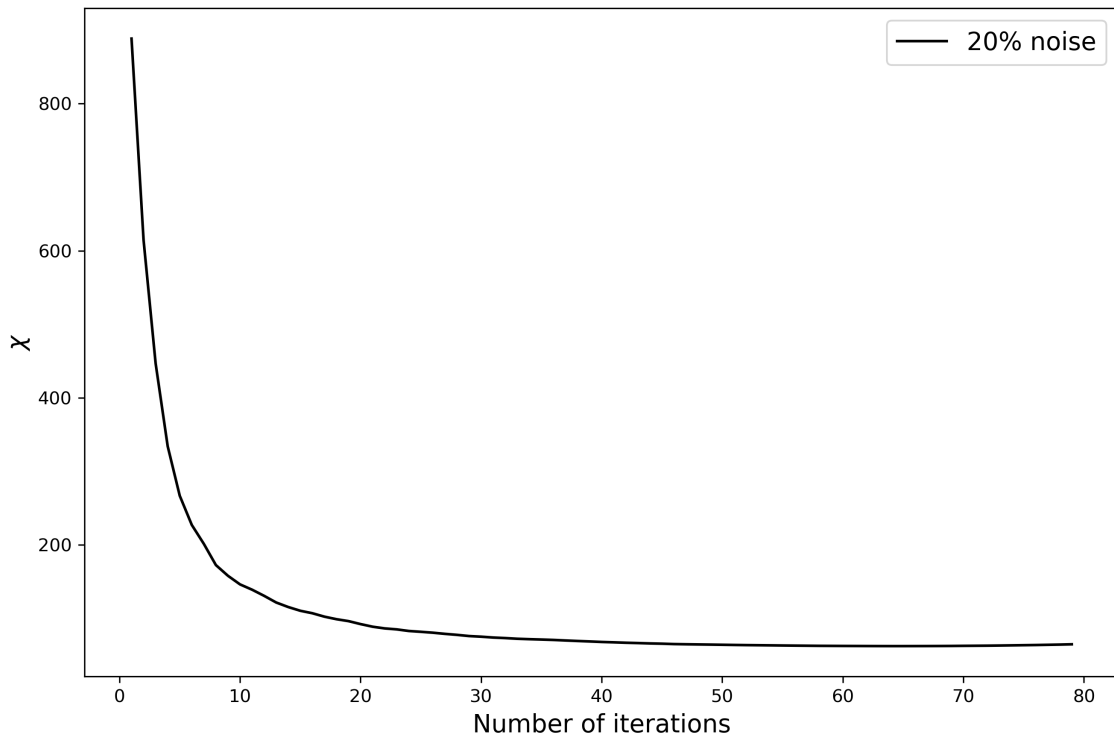


Figure 17: Convergence analysis of the CGLS method for the synthetic application of the magnetic equivalent layer using an irregular grid with 20% of perturbation on the *x-direction* and *y-direction*.

Takahashi, Oliveira Jr. & Barbosa – GEO-XXXX

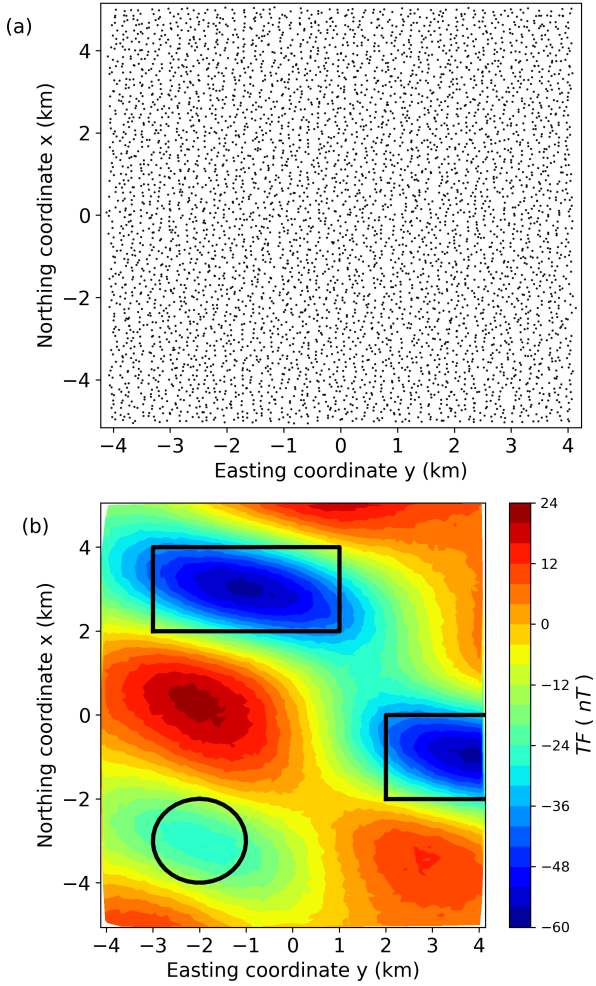


Figure 18: (a) Synthetic magnetic field grid visualization. A irregular grid of  $100 \times 50$  points was used, totaling  $N = 5,000$  observation points. Standard deviations of 30% in the  $x$ -direction and 30% in the  $y$ -direction were applied. (b) Observed synthetic magnetic field data using this irregular grid in panel a. Three bodies were modeled: two prisms and a sphere with inclination, declination and intensity of  $0^\circ$  and  $45^\circ$  and  $2 \times \sqrt{2}$  A/m, respectively.

**Takahashi, Oliveira Jr. & Barbosa – GEO-XXXX**

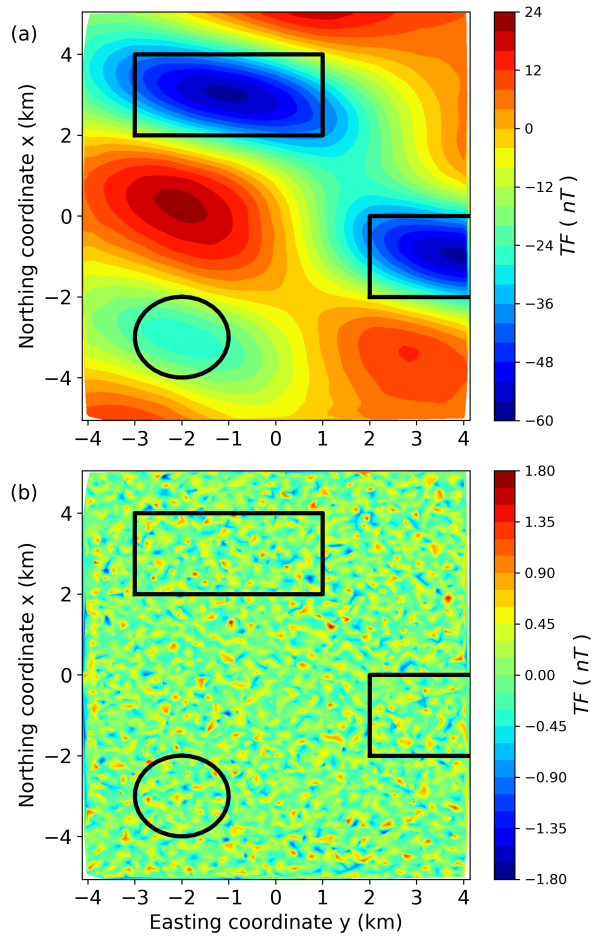


Figure 19: (a) Predicted data using a classical linear inversion method (equation 15) for the irregular grid in figure 18a. (b) Residuals between the observed (18b) and the predicted data (panel a), with mean 0.3634 nT and standart deviation of 0.2735 nT.

Takahashi, Oliveira Jr. & Barbosa – GEO-XXXX

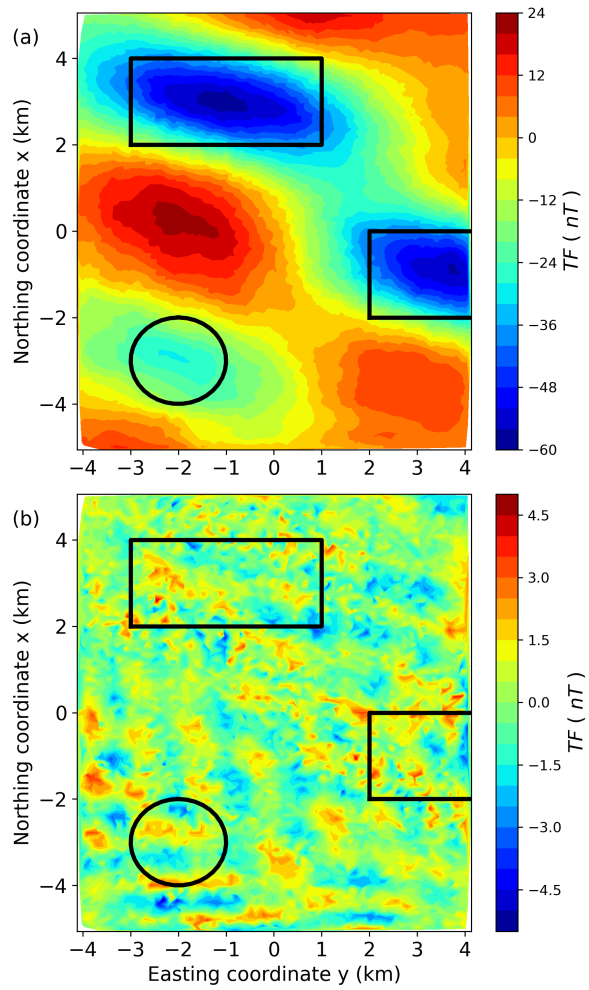


Figure 20: (a) Predicted data using the CGLS method with the fast BTTB matrix-vector product for the irregular grid in figure 18a. (b) Residuals between the observed (18b) and the predicted data (panel a), with mean 0.9788 nT and standard deviation of 0.7462 nT.

Takahashi, Oliveira Jr. & Barbosa – GEO-XXXX

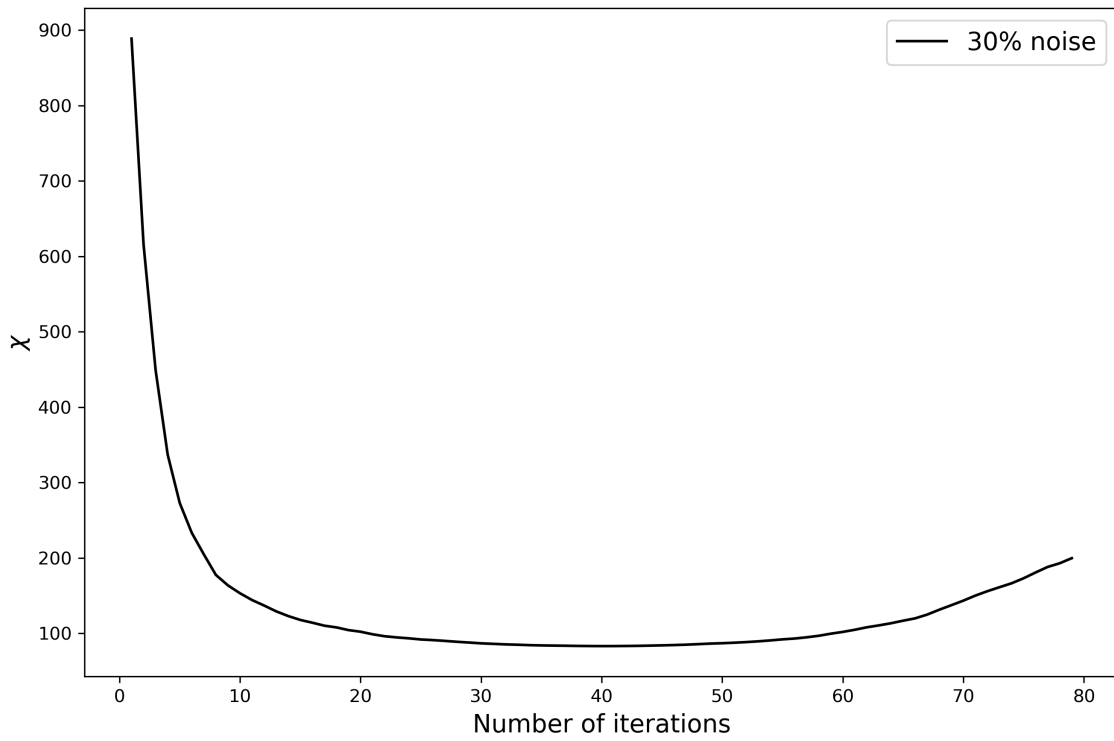


Figure 21: Convergence analysis of the CGLS method for the synthetic application of the magnetic equivalent layer using an irregular grid with 30% of perturbation on the *x-direction* and *y-direction*.

**Takahashi, Oliveira Jr. & Barbosa – GEO-XXXX**

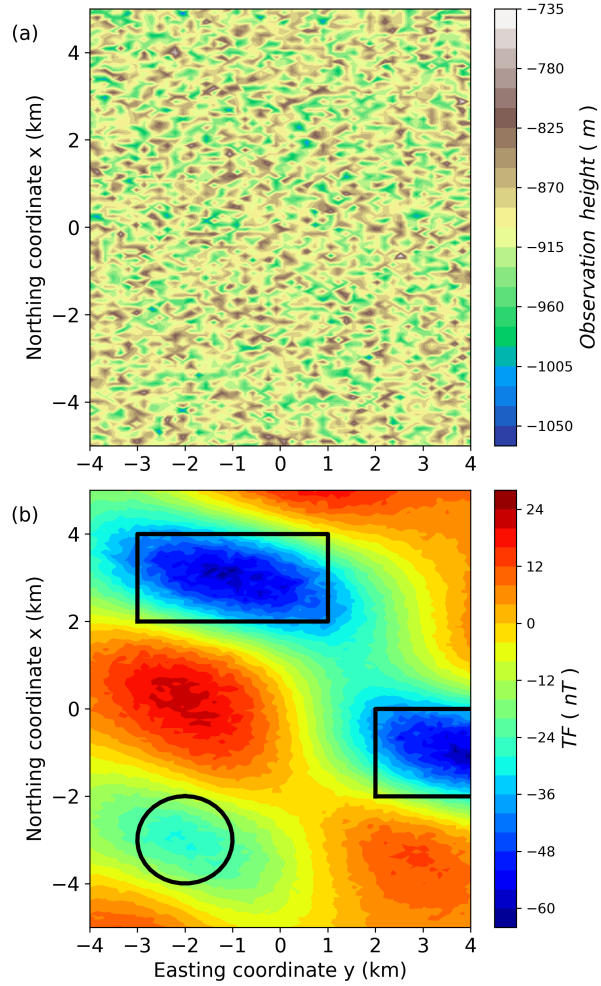


Figure 22: (a) Undulating surface where the total-field anomaly was computed. A irregular grid of  $100 \times 50$  points was used, totaling  $N = 5,000$  observation points. A standart deviation of 5% in the  $z$ -direction was applied. (b) Observed synthetic magnetic field data using this irregular grid in panel a. Three bodies were modeled: two prisms and a sphere with inclination, declination and intensity of  $0^\circ$  and  $45^\circ$  and  $2 \times \sqrt{2}$  A/m, respectively.

Takahashi, Oliveira Jr. & Barbosa – GEO-XXXX

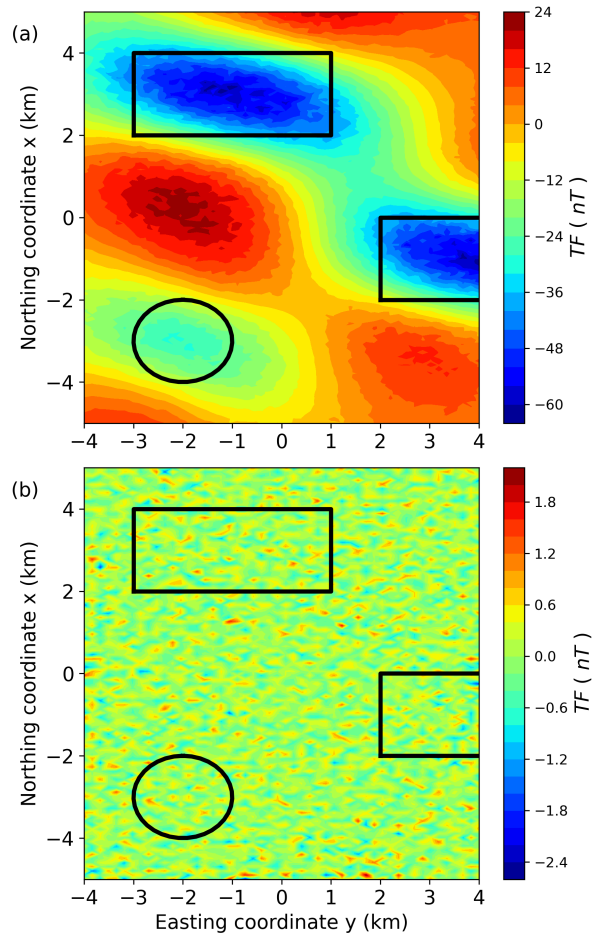


Figure 23: (a) Predicted data using a classical linear inversion method (equation 15) for the irregular grid in figure 22a. (b) Residuals between the observed (22b) and the predicted data (panel a), with mean 0.3712 nT and standart deviation of 0.2870 nT.

Takahashi, Oliveira Jr. & Barbosa – GEO-XXXX

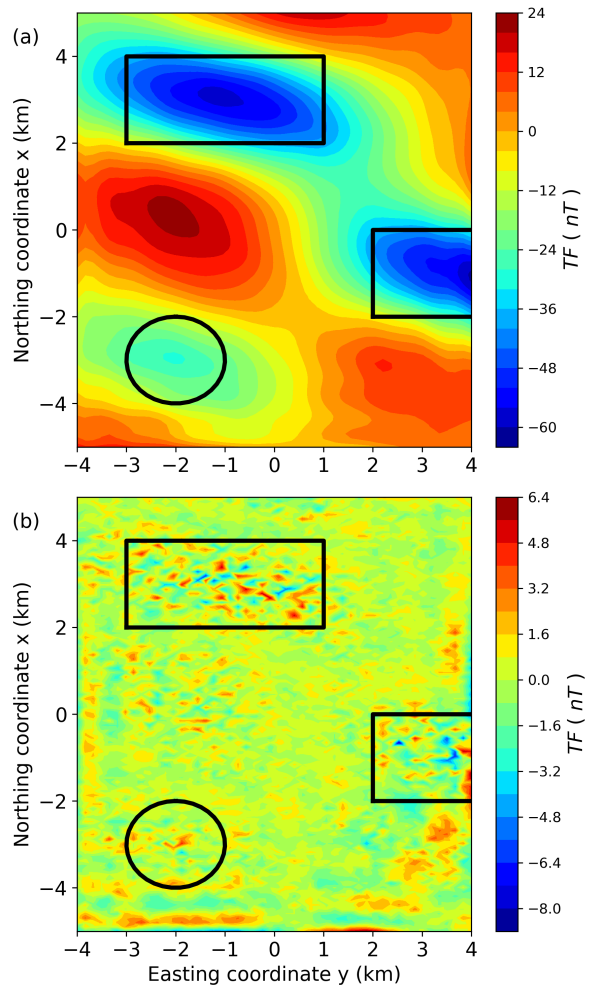


Figure 24: (a) Predicted data using the CGLS method with the fast BTTB matrix-vector product for the irregular grid in figure 22a. (b) Residuals between the observed (22b) and the predicted data (panel a), with mean 0.9542 nT and standard deviation of 0.8943 nT.

Takahashi, Oliveira Jr. & Barbosa – GEO-XXXX

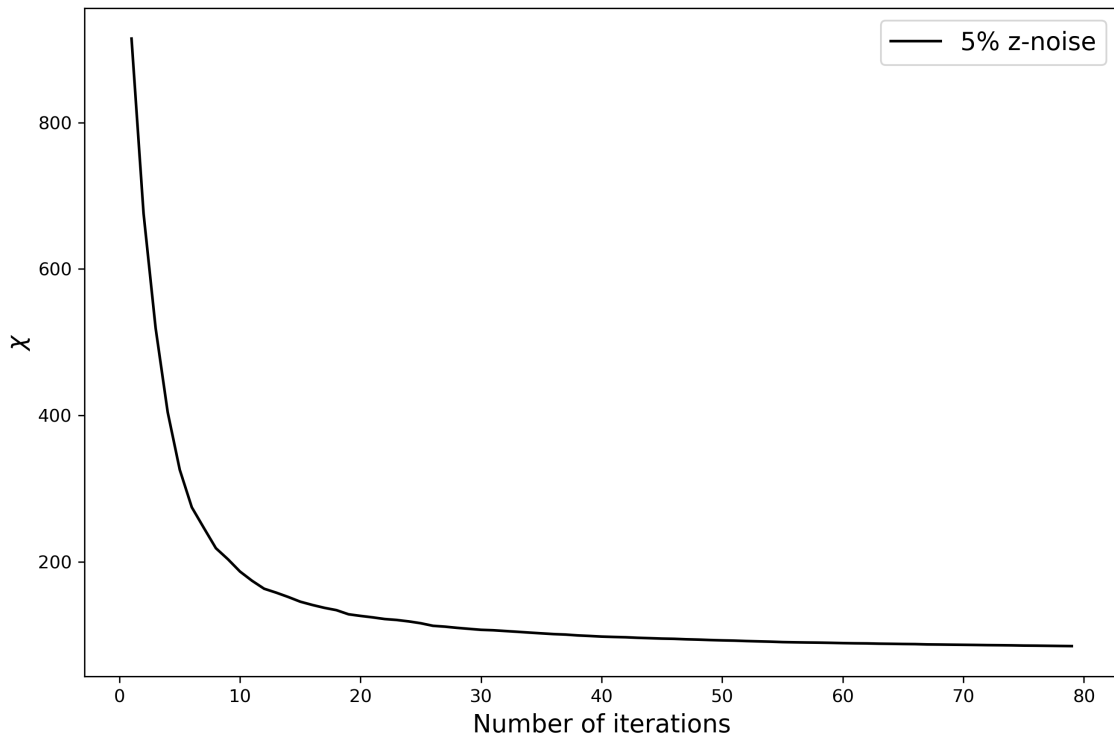


Figure 25: Convergence analysis of the CGLS method for the synthetic application of the magnetic equivalent layer using an irregular grid with 5% of perturbation on the *z-direction*.

Takahashi, Oliveira Jr. & Barbosa – GEO-XXXX

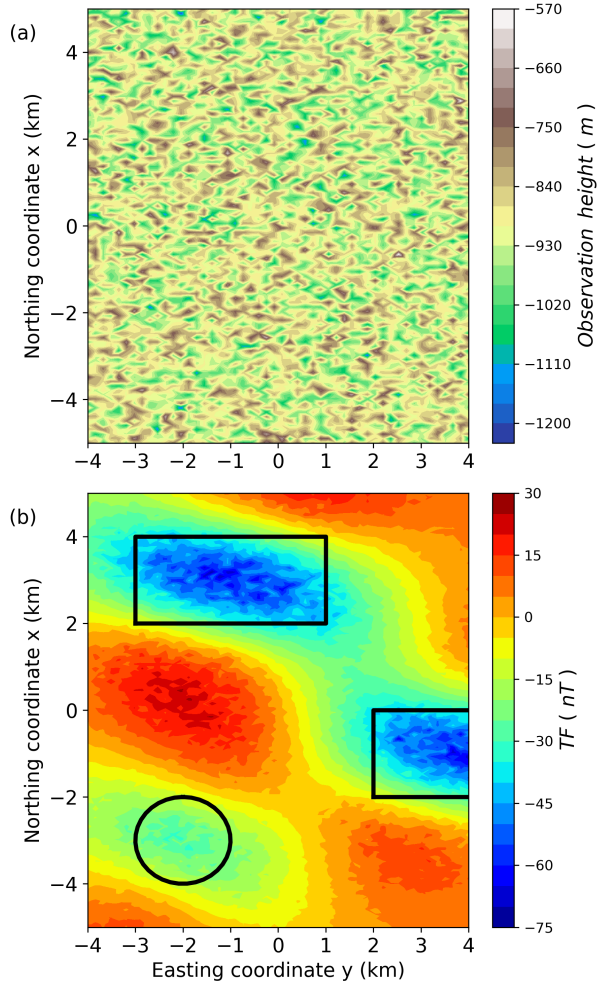


Figure 26: (a) Undulating surface where the total-field anomaly was computed. A irregular grid of  $100 \times 50$  points was used, totaling  $N = 5,000$  observation points. A standart deviation of 10% in the  $z$ -direction was applied. (b) Observed synthetic magnetic field data using this irregular grid in panel a. Three bodies were modeled: two prisms and a sphere with inclination, declination and intensity of  $0^\circ$  and  $45^\circ$  and  $2 \times \sqrt{2}$  A/m, respectively.

Takahashi, Oliveira Jr. & Barbosa – GEO-XXXX

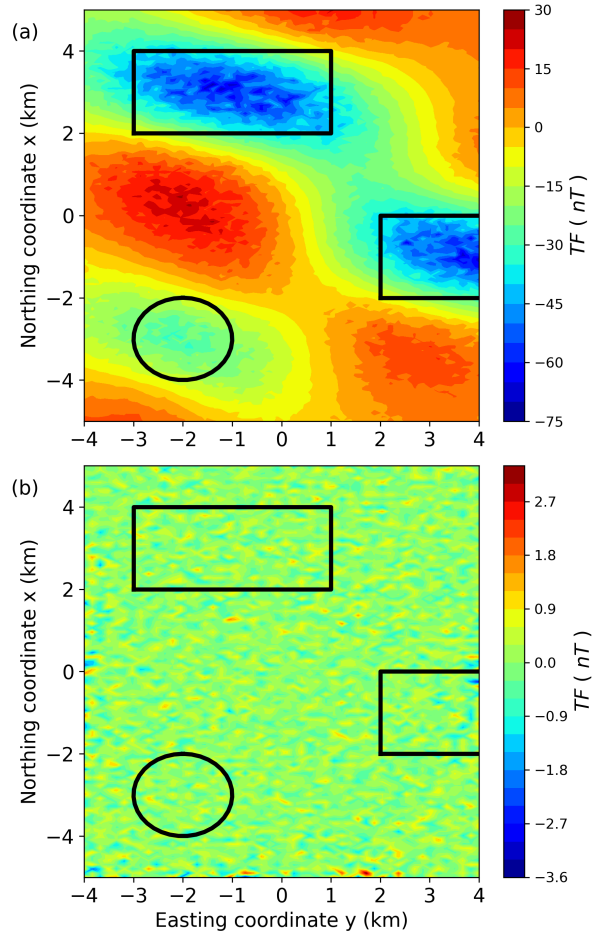


Figure 27: (a) Predicted data using a classical linear inversion method (equation 15) for the irregular grid in figure 26a. (b) Residuals between the observed (26b) and the predicted data (panel a), with mean 0.3865 nT and standart deviation of 0.3216 nT.

Takahashi, Oliveira Jr. & Barbosa – GEO-XXXX

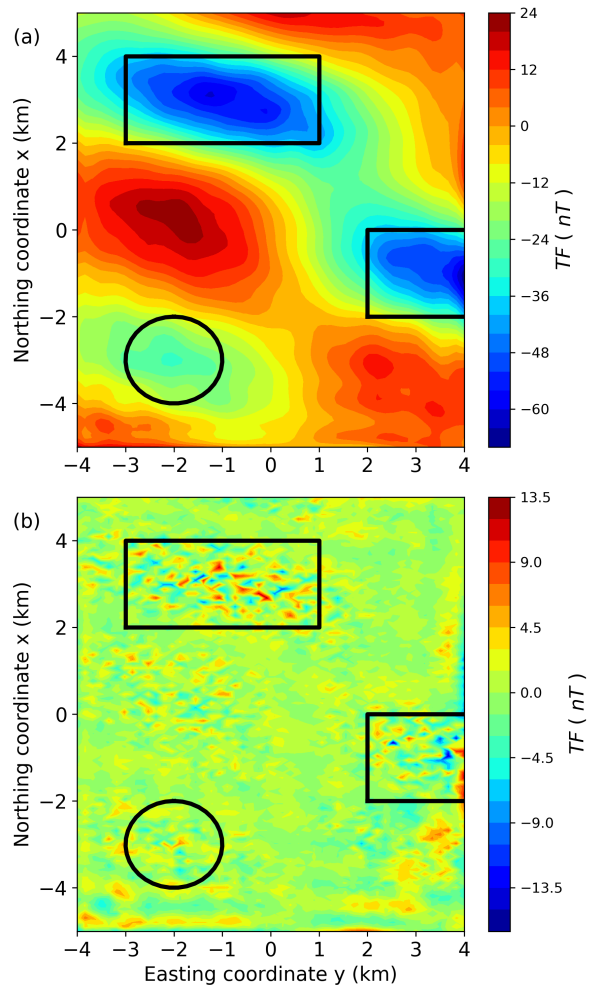


Figure 28: (a) Predicted data using the CGLS method with the fast BTTB matrix-vector product for the irregular grid in figure 26a. (b) Residuals between the observed (26b) and the predicted data (panel a), with mean 1.6105 nT and standard deviation of 1.6231 nT.

Takahashi, Oliveira Jr. & Barbosa – GEO-XXXX

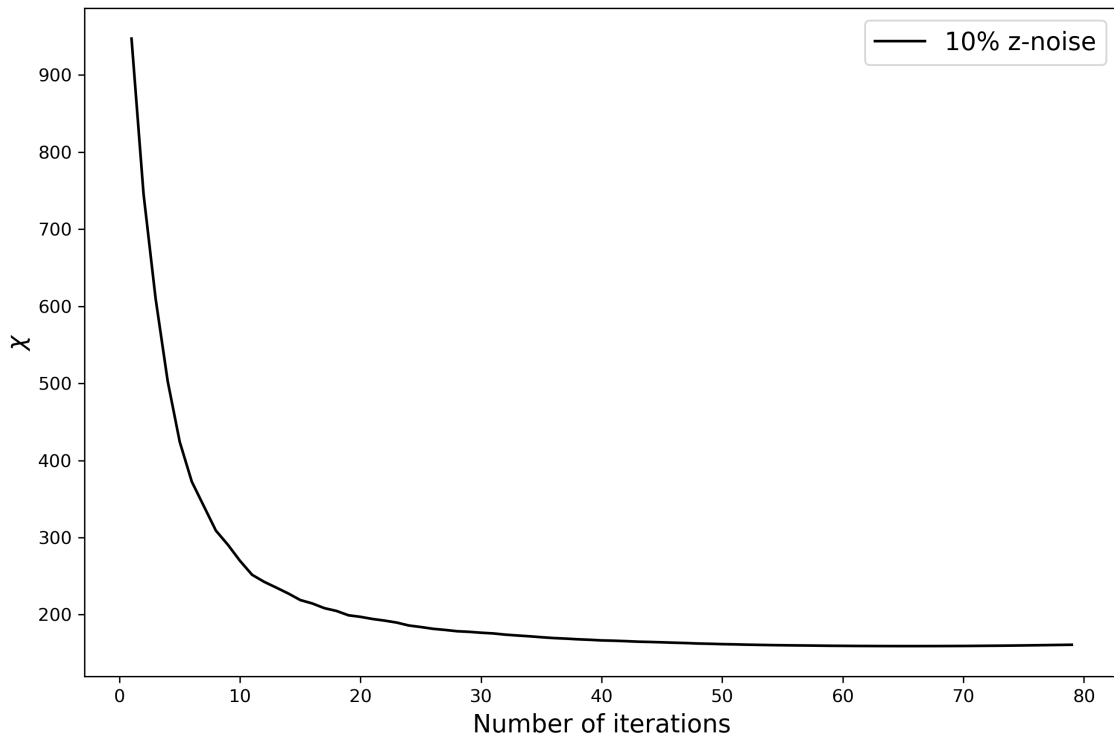


Figure 29: Convergence analysis of the CGLS method for the synthetic application of the magnetic equivalent layer using an irregular grid with 10% of perturbation on the *z-direction*.

Takahashi, Oliveira Jr. & Barbosa – GEO-XXXX

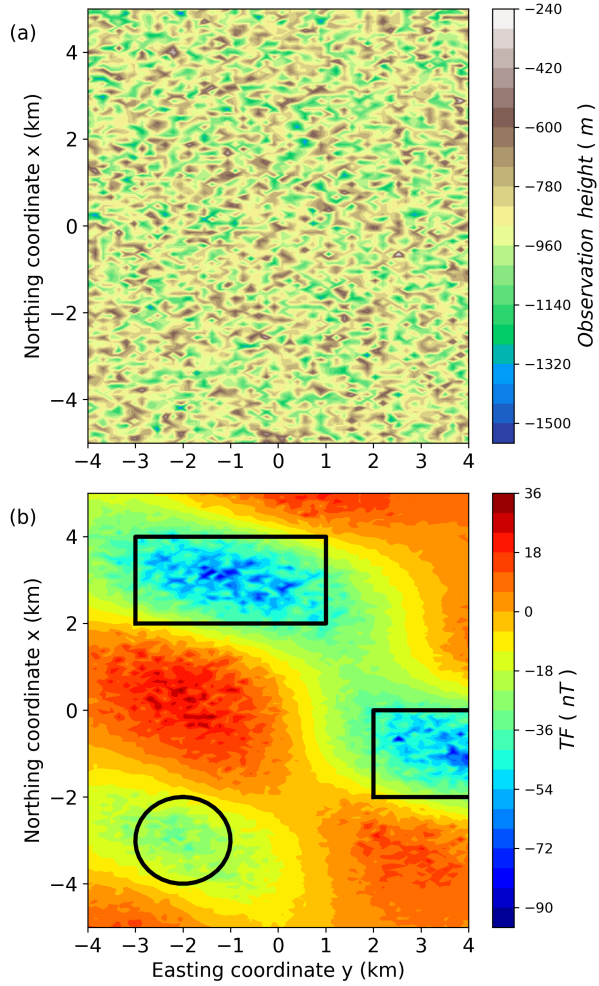


Figure 30: (a) Undulating surface where the total-field anomaly was computed. A irregular grid of  $100 \times 50$  points was used, totaling  $N = 5,000$  observation points. A standart deviation of 20% in the  $z$ -direction was applied. (b) Observed synthetic magnetic field data using this irregular grid in panel a. Three bodies were modeled: two prisms and a sphere with inclination, declination and intensity of  $0^\circ$  and  $45^\circ$  and  $2 \times \sqrt{2}$  A/m, respectively.

Takahashi, Oliveira Jr. & Barbosa – GEO-XXXX

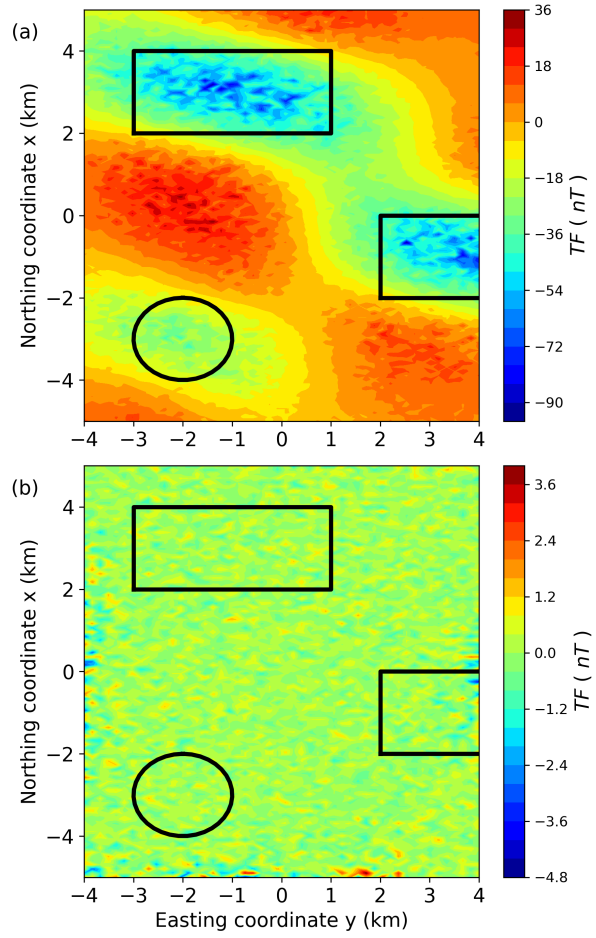


Figure 31: (a) Predicted data using a classical linear inversion method (equation 15) for the irregular grid in figure 30a. (b) Residuals between the observed (30b) and the predicted data (panel a), with mean 0.4155 nT and standart deviation of 0.4005 nT.

**Takahashi, Oliveira Jr. & Barbosa – GEO-XXXX**

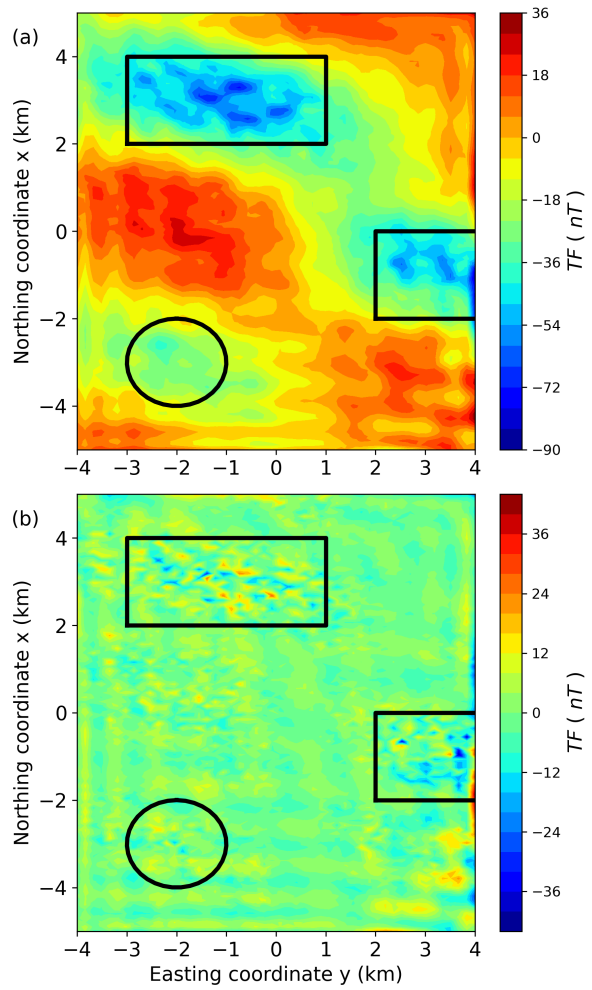


Figure 32: (a) Predicted data using the CGLS method with the fast BTTB matrix-vector product for the irregular grid in figure 30a. (b) Residuals between the observed (30b) and the predicted data (panel a), with mean 6.6220 nT and standard deviation of 5.901 nT.

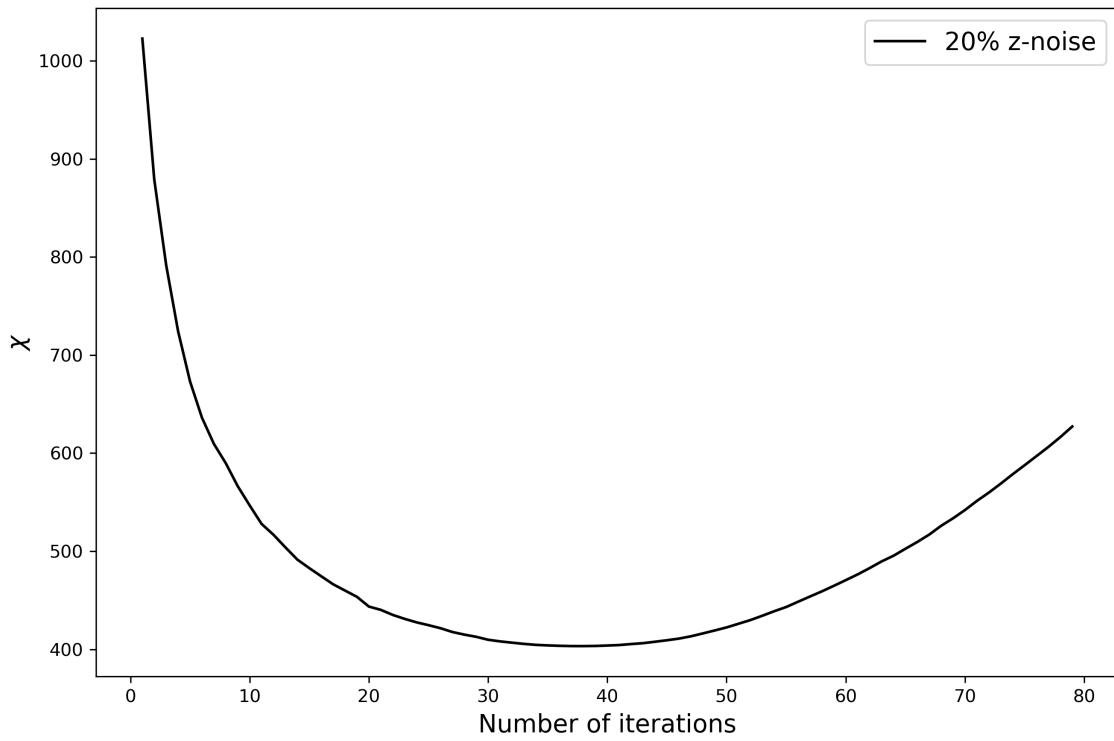


Figure 33: Convergence analysis of the CGLS method for the synthetic application of the magnetic equivalent layer using an irregular grid with 20% of perturbation on the *z-direction*.

Takahashi, Oliveira Jr. & Barbosa – GEO-XXXX

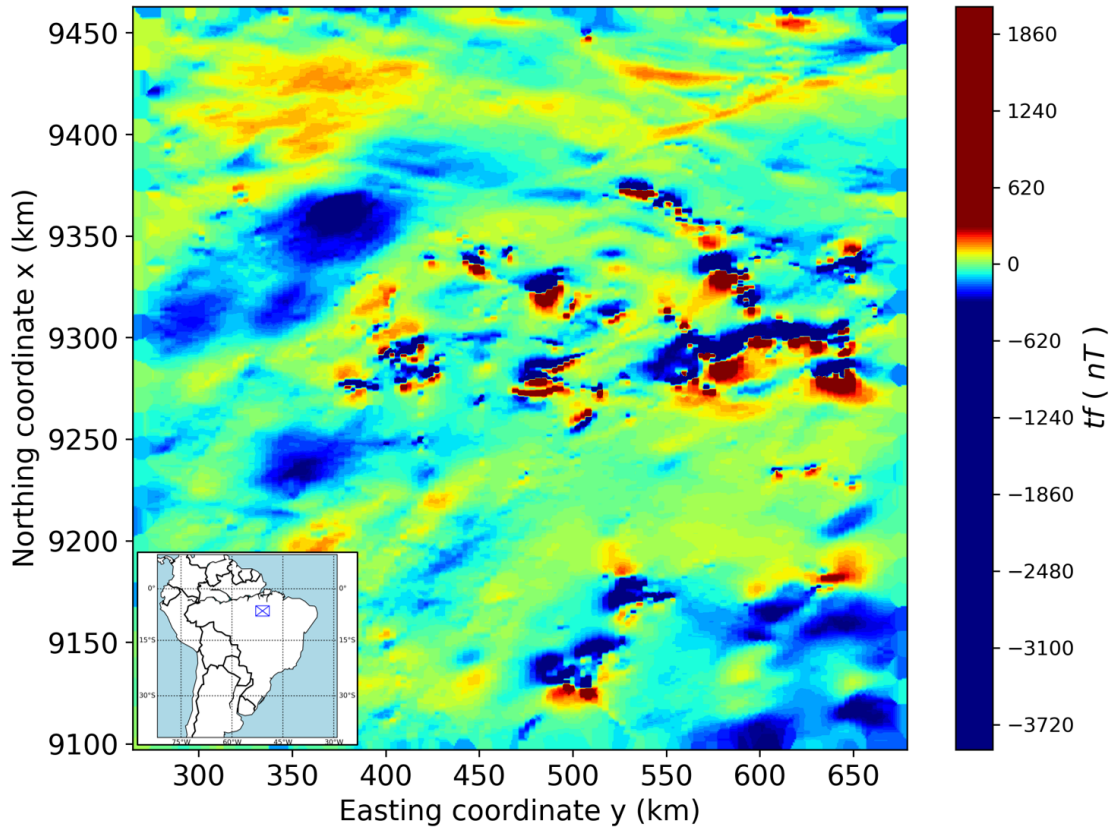


Figure 34: Observed magnetic field data of the Carajás, Brazil area. A regular grid of  $500 \times 500$  points was used, totaling  $N = 250,000$  observation points.

**Takahashi, Oliveira Jr. & Barbosa – GEO-XXXX**

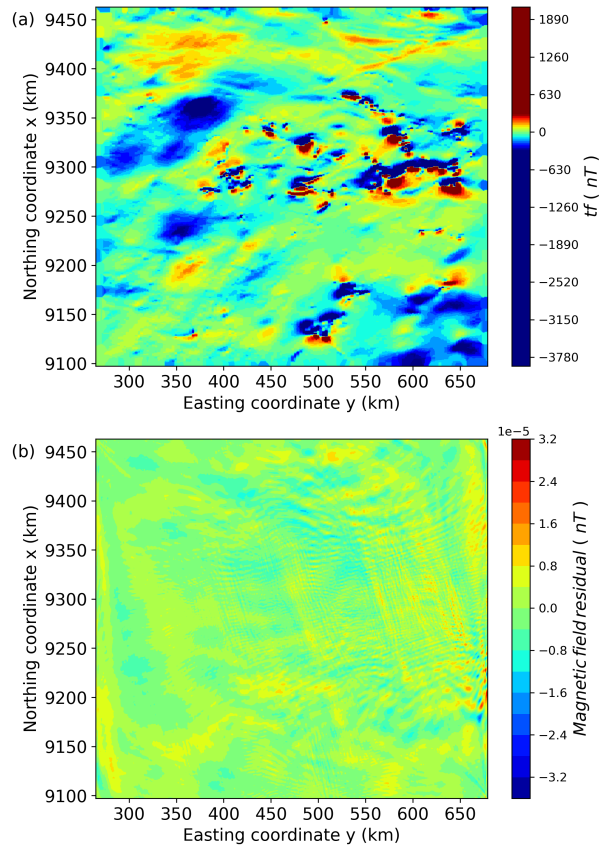


Figure 35: (a) Predicted data using our method. (b) Residuals between the observed (34) and the predicted data (panel a), with mean  $2.4566 \times 10^{-7} \text{ nT}$  and standart deviation of  $1.9787 \times 10^{-6} \text{ nT}$ .

Takahashi, Oliveira Jr. & Barbosa – GEO-XXXX

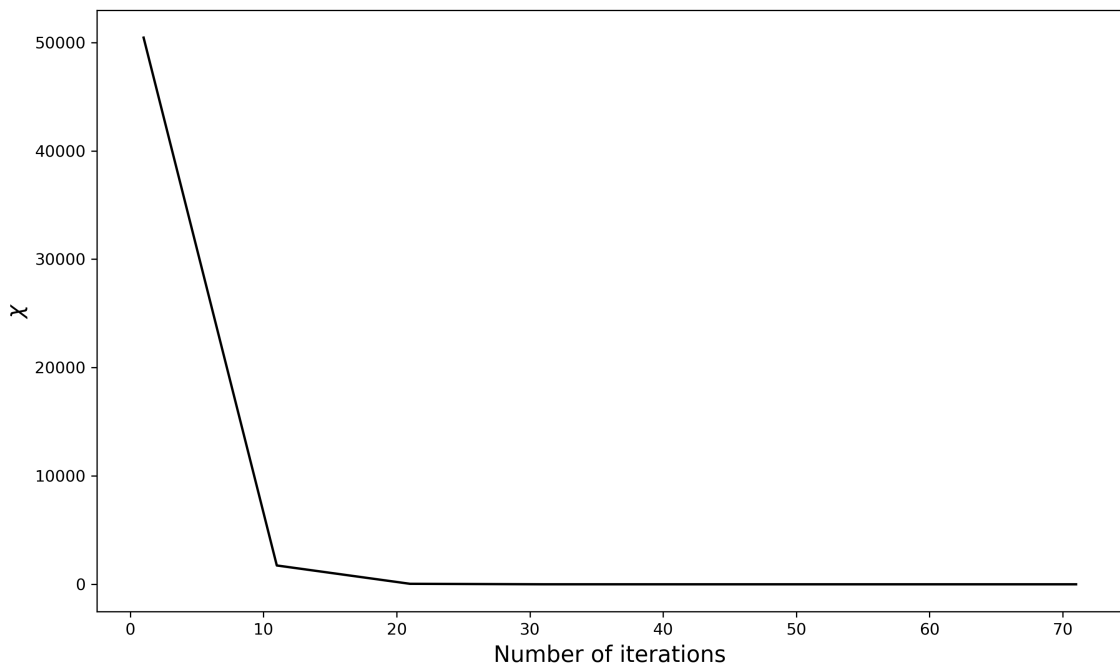


Figure 36: Convergence analysis of the CGLS method for the field data of Carajás, Brazil using the magnetic equivalent layer with a regular grid of  $500 \times 500$  points.

**Takahashi, Oliveira Jr. & Barbosa – GEO-XXXX**

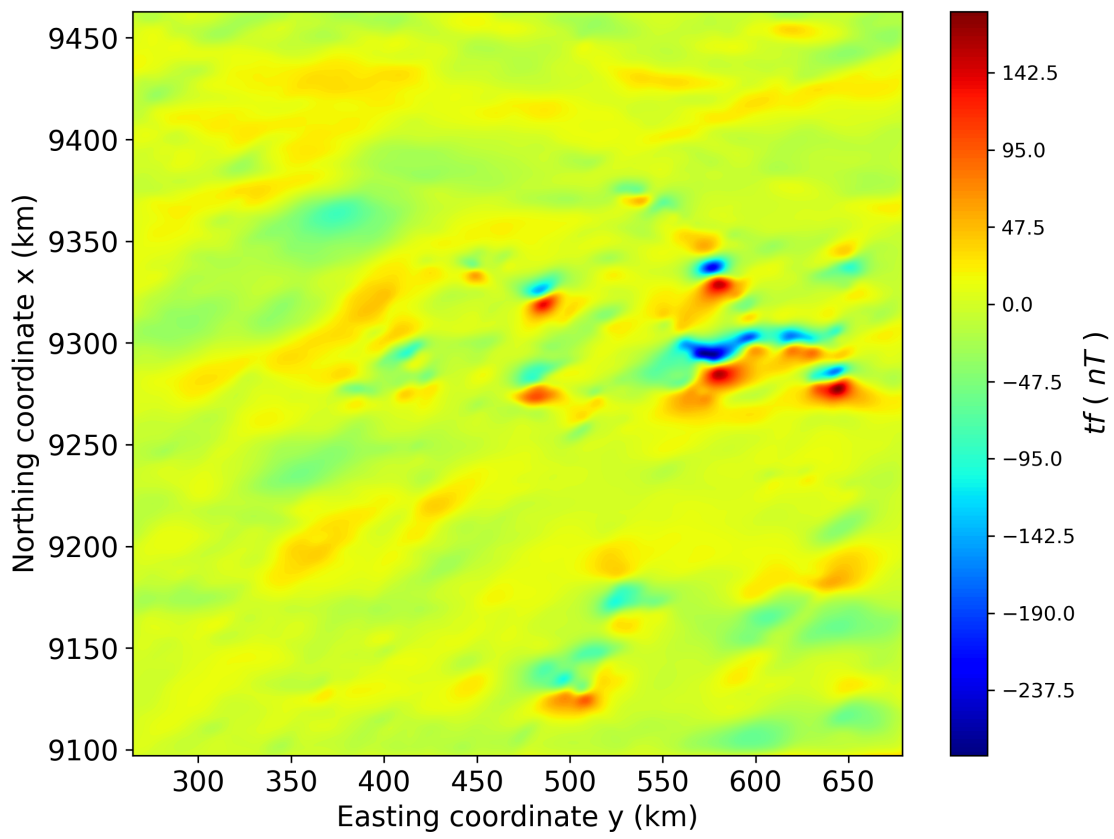


Figure 37: Upward continuation transformation of real data of Carajás, Brazil at 5000 meter. It was necessary 0.49 seconds to complete the process.

**Takahashi, Oliveira Jr. & Barbosa – GEO-XXXX**

$N$	Matrix <b>A</b>	All six first columns of BCCB matrices	Matrix <b>L</b>
100	0.0763	0.0183	0.00610
400	1.22	0.0744	0.0248
2,500	48	0.458	0.1528
10,000	763	1.831	0.6104
40,000	12,207	7.32	2.4416
250,000	476,837	45.768	15.3
500,000	1,907,349	91.56	30.518
1,000,000	7,629,395	183.096	61.035

Table 1: This table shows the RAM memory usage (in Megabytes) for storing the whole matrix **A** (equation 12), the sum of all six first columns of the BCCB matrices embedded from the components of the matrix **H** from equation 10 (both need 8 bytes per element) and the matrix **L** containing the eigenvalues complex numbers (16 bytes per element) resulting from the diagonalization of matrix **C** (equation 63). Here we must consider that  $N$  observation points forms a  $N \times N$  matrix.